The Astrophysical Journal, 868:88 (17pp), 2018 December 1 https://doi.org/10.3847/1538-4357/aaea60

Variability-selected Low-luminosity Active Galactic Nuclei Candidates in the 7 Ms *Chandra* Deep Field-South

N. Ding[1,2,3], B. Luo[1,2,3], W. N. Brandt[4,5,6], M. Paolillo[7,8,9], G. Yang[4,5], B. D. Lehmer[10], O. Shemmer[11], D. P. Schneider[4,5], P. Tozzi[12], Y. Q. Xue[13,14], X. C. Zheng[13,14], Q. S. Gu[1,2,3], A. M. Koekemoer[15], C. Vignali[16,17], F. Vito[4,5], and J. X. Wang[13,14]

[1] School of Astronomy and Space Science, Nanjing University, Nanjing, Jiangsu 210093, People's Republic of China
[2] Key Laboratory of Modern Astronomy and Astrophysics (Nanjing University), Ministry of Education, Nanjing 210093, People's Republic of China
[3] Collaborative Innovation Center of Modern Astronomy and Space Exploration, Nanjing 210093, People's Republic of China
[4] Department of Astronomy and Astrophysics, 525 Davey Lab, The Pennsylvania State University, University Park, PA 16802, USA
[5] Institute for Gravitation and the Cosmos, The Pennsylvania State University, University Park, PA 16802, USA
[6] Department of Physics, 104 Davey Lab, The Pennsylvania State University, University Park, PA 16802, USA
[7] Dipartimento di Fisica Ettore Pancini, Università di Napoli Federico II, via Cintia, I-80126, Italy
[8] INAF—Osservatorio Astronomico di Capodimonte, via Moiariello 16, I-80131, Napoli, Italy
[9] INFN—Unità di Napoli, via Cintia 9, I-80126, Napoli, Italy
[10] Department of Physics, University of Arkansas, 226 Physics Building, 825 West Dickson Street, Fayetteville, AR 72701, USA
[11] Department of Physics, University of North Texas, Denton, TX 76203, USA
[12] INAF—Osservatorio Astrofisico di Firenze, Largo Enrico Fermi 5, I-50125 Firenze, Italy
[13] CAS Key Laboratory for Research in Galaxies and Cosmology, Department of Astronomy, University of Science and Technology of China, Hefei 230026, People's Republic of China
[14] School of Astronomy and Space Science, University of Science and Technology of China, Hefei 230026, People's Republic of China
[15] Space Telescope Science Institute, 3700 San Martin Drive, Baltimore MD 21218, USA
[16] Dipartimento di Fisica e Astronomia, Università degli Studi di Bologna, via Gobetti 93/2, I-40129 Bologna, Italy
[17] INAF—Osservatorio Astronomico di Bologna, via Gobetti 93/3, I-40129 Bologna, Italy
Received 2018 August 31; revised 2018 October 18; accepted 2018 October 20; published 2018 November 27

Abstract

In deep X-ray surveys, active galactic nuclei (AGNs) with a broad range of luminosities have been identified. However, cosmologically distant low-luminosity AGN (LLAGN, $L_X \lesssim 10^{42}$ erg s^{-1}) identification still poses a challenge because of significant contamination from host galaxies. Based on the 7 Ms *Chandra* Deep Field-South (CDF-S) survey, the longest-timescale ($\sim$17 years) deep X-ray survey to date, we utilize an X-ray variability selection technique to search for LLAGNs that remain unidentified among the CDF-S X-ray sources. We find 13 variable sources from 110 unclassified CDF-S X-ray sources. Except for one source that could be an ultraluminous X-ray source, the variability of the remaining 12 sources is most likely due to accreting supermassive black holes. These 12 AGN candidates have low intrinsic X-ray luminosities, with a median value of 7×10^{40} erg s^{-1}. They are generally not heavily obscured, with an average effective power-law photon index of 1.8. The fraction of variable AGNs in the CDF-S is independent of X-ray luminosity and is only restricted by the total number of observed net counts, confirming previous findings that X-ray variability is a near-ubiquitous property of AGNs over a wide range of luminosities. There is an anticorrelation between X-ray luminosity and variability amplitude for high-luminosity AGNs, but as the luminosity drops to $\lesssim 10^{42}$ erg s^{-1}, the variability amplitude no longer appears dependent on the luminosity. The entire observed luminosity–variability trend can be roughly reproduced by an empirical AGN variability model based on a broken power-law power spectral density function.

Key words: galaxies: active – galaxies: nuclei – X-rays: galaxies – X-rays: general

1. Introduction

It is generally believed that a supermassive black hole (SMBH) is located in the center of an active galactic nucleus (AGN). The SMBH provides energy for the AGN by accreting the surrounding material. With a range of X-ray surveys from shallow all-sky surveys to ultradeep pencil-beam surveys, we can obtain a relatively complete census of AGN populations over a wide redshift range (e.g., Brandt & Alexander 2015; Xue 2017). These sensitive X-ray surveys provide an unprecedented opportunity to trace the growth process of SMBHs and investigate the evolution of the AGN luminosity function (e.g., Paolillo et al. 2017; Vito et al. 2018).

In deep X-ray surveys, a source is identified as an AGN according to a number of empirical criteria, for example, a high intrinsic rest-frame X-ray luminosity ($L_X > 3 \times 10^{42}$ erg s^{-1}), a hard X-ray spectrum (effective power-law spectral photon index less than one), or a large ratio of X-ray flux to *R*-band flux ($\log F_X/F_R > -1$; see Xue et al. 2011, 2016; Luo et al. 2017 for details). These selection criteria are successful in selecting AGNs with a broad range of luminosities, but they nevertheless can miss certain populations, such as heavily obscured AGNs and low-luminosity AGNs (see, e.g., Young et al. 2012; Brandt & Alexander 2015; Padovani et al. 2017). Low-luminosity AGNs (LLAGNs) have low X-ray luminosities ($L_X \lesssim 10^{42}$ erg s^{-1}) and often low Eddington accretion rates ($\lambda_{\rm Edd} \ll 0.1$) relative to ordinary AGNs (see, e.g., Ho 2008; Padovani et al. 2017). Despite the lack of violent nuclear activities, they are still a very important AGN population for understanding the transition of accretion modes, the growth of SMBHs, and the coevolution of AGNs and host galaxies (see Ho 2008 for a review). Therefore, it is important to improve the completeness of the census of LLAGNs in deep X-ray surveys. Peterson et al. (2006) simulated *Chandra* observations of nearby low-luminosity

Seyfert nuclei artificially shifted to redshift ∼0.3. Their results suggested that these LLAGNs will exhibit the same X-ray luminosities, spectral shapes, and X-ray-to-optical flux ratios as those of normal or optically bright, X-ray-faint galaxies, which indicates that some cosmologically distant LLAGNs still cannot be identified by relying on the above characteristics (i.e., X-ray luminosity, spectral shape). Cosmologically distant LLAGN identification poses a great challenge.

Variability of the multiwavelength (from radio to γ-ray) radiation is one of the distinctive characteristics of AGNs. Therefore, variability can be used as a tool to select AGNs in extragalactic surveys. For example, Trevese et al. (2008), Morokuma et al. (2008), Villforth et al. (2010), Sarajedini et al. (2011), and De Cicco et al. (2016, 2018, in preparation) used optical variability to select AGNs from the 1 Ms *Chandra* Deep Field-South (CDF-S), the *Subaru/XMM-Newton* Deep Field, the GOODS-North Field, the GOODS-South Field, and the VST-SUDARE survey of the COSMOS Field, respectively. Because AGNs are more variable in the X-ray band than in the UV/optical band, and AGN emission in the X-ray band has relatively less contamination from non-AGN systems, X-ray variability can be effectively used as a tool to identify LLAGNs (e.g., Young et al. 2012). The variability of AGNs generally presents "red noise" behavior, namely the occurrence of larger amplitude variations on longer timescales (e.g., Lawrence et al. 1987; McHardy et al. 2006). As such, AGN variability is more easily detected in a longer observational time span (see, e.g., Lanzuisi et al. 2014; Padovani et al. 2017). Young et al. (2012) utilized the X-ray variability selection technique to search for AGN candidates missed by other selection criteria in the 4 Ms CDF-S (Xue et al. 2011). They reported that 20 CDF-S galaxies have long-term X-ray variability, and 19 of them are LLAGNs.

Recently, the 7 Ms CDF-S survey, the deepest X-ray survey to date, was presented in Luo et al. (2017). This survey data set provides a lengthy observational time span (∼17 years) and a large number of observed net counts for the X-ray sources, improving our ability to detect X-ray variability. Therefore, we use the 7 Ms CDF-S data to search for LLAGNs from unclassified X-ray sources in the CDF-S. This paper is organized as follows. Section 2 describes data processing and sample selection. Section 3 presents the method and results of searching for variable X-ray sources. We further select LLAGN candidates from these variable X-ray sources and report their basic properties in Section 4. In Section 5 we discuss the efficiency of X-ray variability selection of LLAGNs and the fraction of variable AGNs in the CDF-S, and we also explore the relation between X-ray luminosity and variability amplitude for long-term AGN variability. Section 6 summarizes the main results of this work. Cosmological parameters of $H_0 = 70\,\mathrm{km\,s^{-1}\,Mpc^{-1}}$, $\Omega_m = 0.3$, and $\Omega_\Lambda = 0.7$ (Planck Collaboration et al. 2016) and a Chabrier initial mass function (IMF; Chabrier 2003) are adopted in this work.

2. Data and Sample

This study is based on the 7 Ms CDF-S data (Luo et al. 2017). The data set consists of 102 observations collected by the *Chandra* Advanced CCD Imaging Spectrometer imaging array (ACIS-I; Garmire et al. 2003) from 1999 October to 2016 March, and the cumulative observed exposure time is nearly 7 Ms. We divide the CDF-S observations into seven epochs according to the distribution of the observation times (see Table 1 for details); the first four epochs are the same as those in Young et al. (2012). Each epoch spans several months to one year and has approximately 1 Ms combined exposure time. This binning strategy enhances the signal-to-noise ratio for faint sources while minimizing the influence of broad time-span bins on variability.

The 7 Ms CDF-S main catalog contains 1008 X-ray sources, of which 711 are classified as AGNs. Excluding 12 stars, the remaining 285 unclassified X-ray sources are considered as normal galaxies (see Luo et al. 2017 for details). To perform reliable variability analyses, we construct a sample based on the following four criteria:

1. The source has an off-axis angle of $<8'$.
2. The source has at least 30 net 0.5–7 keV counts in the full 7 Ms exposure.
3. The source is not one of the six transient events identified by Zheng et al. (2017).
4. The source has redshift measurements.

The first criterion ensures that each source is well covered by all observations. The second criterion excludes sources with extremely weak X-ray emission to improve the reliability of variability analyses. The third criterion excludes transient events because they are probably not bona fide AGNs. Five sources satisfy the first two criteria but do not meet the third criterion. Their XIDs[18] are 297, 330, 403, 725, and 935. They have all been classified as AGNs in Luo et al. (2017). This conservative criterion (i.e., excluding the five controversial AGNs from the AGN sample) does not materially affect the results of our following analyses. The fourth criterion enables us to calculate X-ray luminosity for each source. Six sources are excluded from the sample based on this criterion. The six sources have all been classified as AGNs in Luo et al. (2017), and they are unlikely to be LLAGNs at low redshifts. We obtain a final sample containing 505 sources, of which 395 are AGNs and 110 are unclassified X-ray sources. These unclassified X-ray sources are considered normal galaxies in Luo et al. (2017) but may actually contain unidentified LLAGNs, and they are the main subject investigated in this paper. We examine the variability of the 395 AGNs for comparison purposes in Section 5. We use ACIS Extract (AE; Broos et al. 2010)[19] to extract source photometry in each epoch. The extracted full-band (0.5–7 keV) photometry is utilized to analyze variability.[20]

3. Searching for Variable X-Ray Sources

In this section, we search for variable X-ray sources among the 110 unclassified X-ray sources. These variable X-ray sources will be investigated further in the next section (Section 4) regarding whether their X-ray variability is due to accreting SMBHs.

3.1. Method

We assess whether a source has X-ray variability according to the probability that its observed X-ray photon-flux

[18] XID in the entire paper refers to the source sequence number in the 7 Ms main catalog.

[19] See http://personal.psu.edu/psb6/TARA/AE.html for details on ACIS Extract.

[20] We only use the full-band data (instead of soft-band or hard-band data) to analyze variability, because the largest number of net counts in the full band for a given source improves the likelihood and reliability of variability detection.

Table 1
Details of the Seven Epochs

Epoch	Observation date range and observation IDs	Total exposure time (ks)
1	1999.10–2000.12	930.8
	1431-0 1431-1 441 582 2406 2405 2312 1672 2409 2313 2239	
2	2007.09–2007.11	959.9
	8591 9593 9718 8593 8597 8595 8592 8596 9575 9578 8594 9596	
3	2010.03–2010.05	1012.6
	12043 12123 12044 12128 12045 12129 12135 12046 12047 12137 12138 12055 12213 12048	
4	2010.05–2010.07	943.3
	12049 12050 12222 12219 12051 12218 12223 12052 12220 12053 12054 12230 12231 12227 12233 12232 12234	
5	2014.06–2014.10	931.4
	16183 16180 16456 16641 16457 16644 16463 17417 17416 16454 16176 16175 16178 16177 16620 16462	
6	2014.10–2015.01	922.2
	17535 17542 16184 16182 16181 17546 16186 16187 16188 16450 16190 16189 17556 16179 17573	
7	2015.03–2016.03	1026.8
	17633 17634 16453 16451 16461 16191 16460 16459 17552 16455 16458 17677 18709 18719 16452 18730 16185	

fluctuation is generated by Poisson noise alone (e.g., Young et al. 2012; Yang et al. 2016; Paolillo et al. 2017).

We utilize the statistic

$$X^2 = \sum_{i=1}^{7} \frac{(\mathrm{PF}_i - \langle \mathrm{PF} \rangle)^2}{(\delta \mathrm{PF}_i)^2} \quad (1)$$

to measure X-ray photon-flux fluctuation, where i indicates different epochs (1–7), PF_i is the photon flux in each epoch, and $\langle \mathrm{PF} \rangle$ is the measured photon flux from the stacked 7 Ms data. The photon flux in each epoch is calculated as

$$\mathrm{PF}_i = \frac{\mathrm{NET\_CNTS}_i}{\mathrm{EFFAREA}_i \times \mathrm{EXPOSURE}_i \times \mathrm{PSF\_FRAC}_i}, \quad (2)$$

and its 1σ uncertainty is

$$\delta \mathrm{PF}_i = \frac{\delta \mathrm{NET\_CNTS}_i}{\mathrm{EFFAREA}_i \times \mathrm{EXPOSURE}_i \times \mathrm{PSF\_FRAC}_i}, \quad (3)$$

where $\mathrm{NET\_CNTS}_i$ is the background-subtracted counts (i.e., net counts); $\delta\mathrm{NET\_CNTS}_i$ is the uncertainty on the net counts, which is the mean of the upper and lower 1σ errors;[21] and the $\mathrm{EFFAREA}_i$, $\mathrm{EXPOSURE}_i$, and $\mathrm{PSF\_FRAC}_i$ parameters are the effective area, exposure time, and point-spread function (PSF) fraction calculated by AE, respectively. The effective area takes into account the varying sensitivity of *Chandra* observations between the different epochs (e.g., due to vignetting, CCD gaps, quantum-efficiency degradation).

For a nonvariable source, its observed photon-flux fluctuation is entirely due to Poisson noise. When the count rate of such a source is high ($\gtrsim$15 net counts in each epoch; e.g., Young et al. 2012), the X^2 value of its photon-flux fluctuation will follow a χ^2 distribution with six degrees of freedom. However, when the count rate is low ($\lesssim$15 in each epoch), the X^2 value will deviate from the χ^2 distribution because the errors on the net counts are not Gaussian (e.g., Paolillo et al. 2004). In our sample, most sources have low counts in each epoch bin. Therefore, we use Monte Carlo simulations to obtain the X^2 value of photon-flux fluctuation produced by Poisson noise alone (e.g., Paolillo et al. 2004; Young et al. 2012; Yang et al. 2016; Paolillo et al. 2017). By comparing the measured X^2 value to the X^2 values generated from the simulations, we can obtain the probability that the observed photon-flux fluctuation is produced by Poisson noise alone. The specific process is described as follows.

In each simulation, we assume that the source is nonvariable and PF remains constant in all seven epochs. The exact value of PF should be the measured $\langle \mathrm{PF} \rangle$ value modified by its statistical uncertainty. We test to consider the effects of uncertainty on $\langle \mathrm{PF} \rangle$ and find that these have a negligible effect on the simulation result. Therefore, we simply adopt the measured $\langle \mathrm{PF} \rangle$ as PF in each simulation. Once the PF value is determined, the model net counts, model background counts, and model source counts are calculated as

$$\mathrm{NET\_CNTS}_i^{\mathrm{model}} = \langle \mathrm{PF} \rangle \times \mathrm{EFFAREA}_i \times \mathrm{EXPOSURE}_i \times \mathrm{PSF\_FRAC}_i, \quad (4)$$

$$\mathrm{BKG\_CNTS}_i^{\mathrm{model}} = \mathrm{BKG\_CNTS}_i^{\mathrm{observed}}, \quad (5)$$

$$\mathrm{SRC\_CNTS}_i^{\mathrm{model}} = \mathrm{NET\_CNTS}_i^{\mathrm{model}} + \frac{\mathrm{BKG\_CNTS}_i^{\mathrm{model}}}{\mathrm{BACKSCAL}_i}, \quad (6)$$

where $\mathrm{BACKSCAL}_i$ is the area ratio of the background-extraction aperture to the source-extraction aperture. We simulate the observed source counts (background counts) by randomly sampling from a Poisson distribution with a mean value of $\mathrm{SRC\_CNTS}_i^{\mathrm{model}}$ ($\mathrm{BKG\_CNTS}_i^{\mathrm{model}}$). We then extract source photometry (net counts and errors) following the algorithm in AE and calculate the X^2 value of the simulated data using Equations (1)–(3). The simulations are performed 10,000 times to obtain 10,000 X^2 values. By comparing the distribution of these simulated X^2 values to the X^2 value of the observed photon-flux fluctuation, we obtain the proportion of the simulated X^2 values greater than the measured X^2 value. This proportion represents the probability (P_{X^2}) that the observed photon-flux fluctuation is generated by Poisson noise alone. For a given source, if none of its 10,000 simulated X^2 values is larger than its measured X^2 value, we obtain a 90% confidence level upper limit on its P_{X^2} value, that is, $P_{X^2} < 0.0002$ (Gehrels 1986).

[21] The upper and lower 1σ errors are calculated following Gehrels (1986).

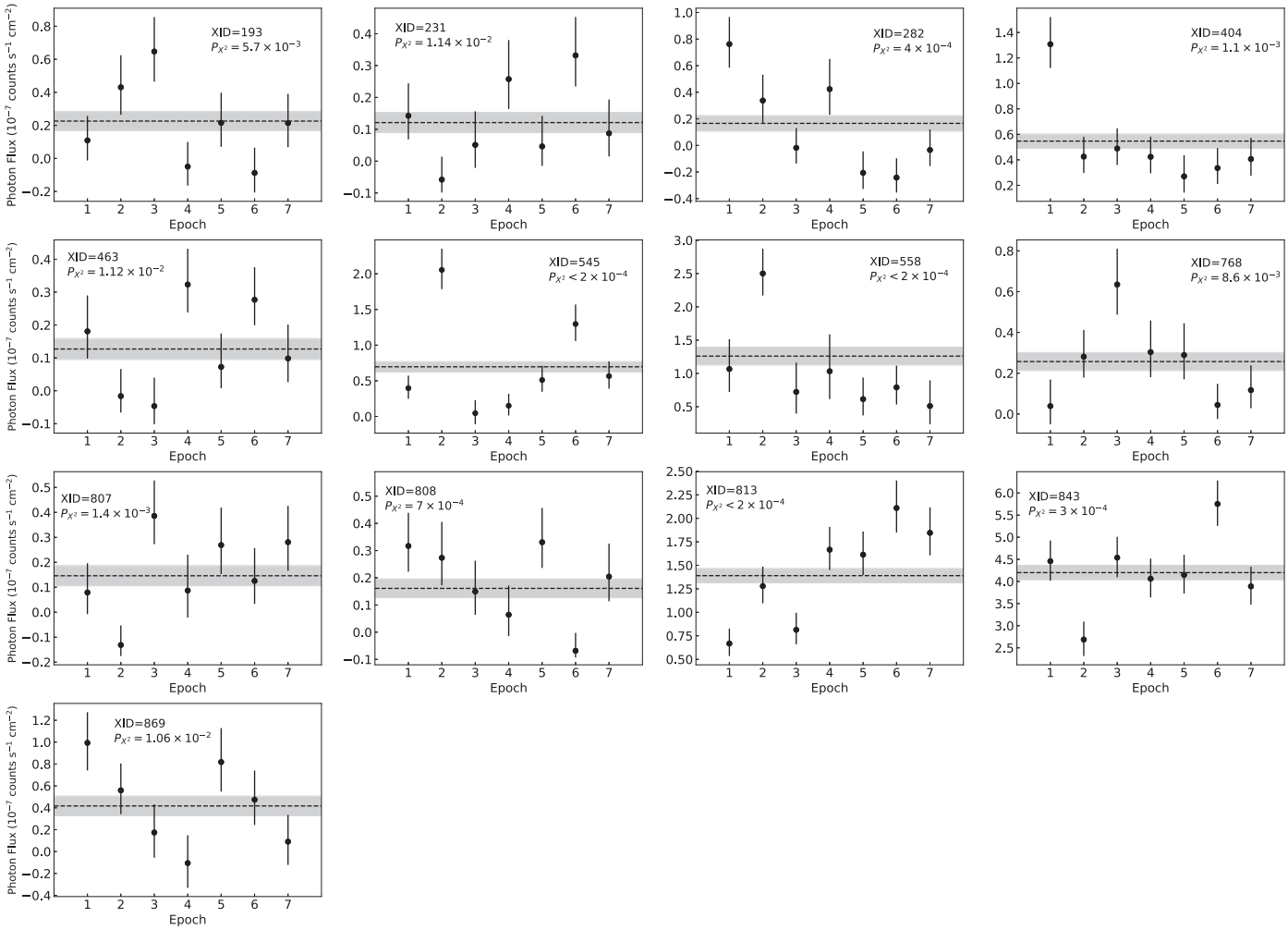

Figure 1. Light curves for the 13 variable X-ray sources. In each panel, the black dashed line is the photon flux of the source from the stacked 7 Ms data, and the gray shaded area represents its 1σ error. The labels in each panel are the source sequence number (XID) in the 7 Ms main catalog and the P_{X^2} value. Note that the seven epochs are not spaced evenly in time (see Table 1).

Table 2
Properties of the 13 Variable CDF-S X-Ray Sources

XID	z	Net counts	$\log L_{0.5-7\mathrm{keV,int}}$ (erg s^{-1})	X^2	P_{X^2}	$\sigma^2_{\mathrm{NXS,corr}}$	SFR ($M_\odot$ yr^{-1})	$\log M_\star$ ($M_\odot$)	Γ_{eff}
(1)	(2)	(3)	(4)	(5)	(6)	(7)	(8)	(9)	(10)
193	0.085	57.6	39.5	18.1	0.0057	0.57 ± 0.45	1.41	9.3	1.4
231	0.333	32.3	40.5	17.6	0.0114	0.51 ± 0.45	0.44	8.7	1.6
282	0.674	40.6	41.5	35.6	0.0004	4.43 ± 1.81	4.68	10.2	3.0
404	0.131	138.4	40.3	22.7	0.0011	0.34 ± 0.27	0.28	9.0	$1.24^{+0.21}_{-0.19}$
463	0.834	34.0	41.5	17.9	0.0112	0.64 ± 0.38	11.12	9.4	2.6
545	0.668	175.8	42.1	61.0	<0.0002	1.28 ± 0.61	45.71	10.1	$1.12^{+0.21}_{-0.20}$
558	0.075	119.5	39.8	27.8	<0.0002	0.21 ± 0.13	5.49	9.9	$1.88^{+0.25}_{-0.25}$
768	0.147	63.3	39.9	17.5	0.0086	0.34 ± 0.28	0.33	8.9	$2.01^{+0.51}_{-0.50}$
807	0.496	36.7	40.9	26.8	0.0014	0.23 ± 0.53	0.12	10.8	1.8
808	0.738	43.5	41.4	33.1	0.0007	0.05 ± 0.31	12.88	9.9	2.1
813	0.414	369.1	41.8	48.9	<0.0002	0.12 ± 0.04	7.41	10.2	$1.53^{+0.11}_{-0.11}$
843	0.103	983.5	40.8	25.7	0.0003	0.03 ± 0.02	0.09	11.0	$1.98^{+0.09}_{-0.10}$
869	0.077	101.0	39.7	15.7	0.0106	0.34 ± 0.26	0.05	8.2	1.5

Note. Columns: (1) Sequence number in the 7 Ms CDF-S main catalog (Luo et al. 2017). (2) Spectroscopic redshift. (3) Total number of net counts in the 0.5–7 keV band. (4) Logarithm of the intrinsic rest-frame 0.5–7 keV luminosity from Luo et al. (2017). (5) Variability statistic. (6) Probability that the measured variability is due to Poisson noise alone. (7) Normalized excess variance corrected for sampling bias and its 1σ uncertainty. (8) Star formation rate from Santini et al. (2015). (9) Logarithm of stellar mass from Santini et al. (2015). (10) Effective power-law photon index and its 1σ lower and upper uncertainties from Luo et al. (2017). For sources detected only in the soft or hard bands, a best-guess value of the effective power-law photon index was estimated from the Bayesian code BEHR, and it has no error estimate.

Table 3
Properties of the Five Lower-significance Variable Sources with $0.015 < P_{X^2} < 0.05$

XID	z	Net counts	$\log L_{0.5-7\mathrm{keV,int}}$ (erg s^{-1})	X^2	P_{X^2}	$\sigma^2_{\mathrm{NXS,corr}}$	SFR ($M_\odot$ yr^{-1})	$\log M_\star$ ($M_\odot$)	Γ_{eff}
(1)	(2)	(3)	(4)	(5)	(6)	(7)	(8)	(9)	(10)
80	0.575	224.2	42.0	12.3	0.0373	0.01 ± 0.07	...	...	1.5
219	0.576	40.2	41.1	12.0	0.0444	0.26 ± 0.33	34.88	10.2	2.0
553	0.076	289.0	40.0	12.8	0.0336	0.01 ± 0.02	6.03	10.0	$2.62^{+0.26}_{-0.28}$
663	0.542	33.0	41.0	16.1	0.0215	-0.17 ± 0.24	10.23	9.7	1.4
825	0.438	56.1	40.9	12.9	0.0337	0.11 ± 0.14	14.45	10.1	1.8

Note. The same format as Table 2 but for the five lower-significance variable sources with $0.015 < P_{X^2} < 0.05$. Measurements of star formation rate and stellar mass are not available for XID 80. Statistically, three to four sources among the five objects are expected to be false-positive detections. See Section 3.2 for details.

3.2. Results

The P_{X^2} values of the 110 unclassified CDF-S X-ray sources are calculated using the above method. We adopt $P_{X^2} < 0.015$ as the threshold for selecting variable sources. This conservative selection criterion (compared to $P_{X^2} < 0.05$ in Young et al. 2012) is chosen to balance the need to recover a significant number of true variable sources while keeping the number of false-positive sources relatively small. We find 13 variable sources from the 110 objects (see Table 2), of which one to two variable sources are theoretically expected to be false positives according to the selection criterion ($P_{X^2} < 0.015$). The 13 variable sources account for $\approx 12^{+4}_{-2}\%$ of the total number of the unclassified X-ray sources, where the binomial errors on the fraction at a 1σ confidence level are calculated following Cameron (2011). The light curves of the 13 variable sources are shown in Figure 1.

For completeness, we also list five lower-significance variable sources with $0.015 < P_{X^2} < 0.05$ in Table 3. Statistically, we expect that three to four sources among these five objects are false-positive detections. In the following analyses, we do not treat these five objects as variable sources.

3.3. Comparison with Previous Results

Young et al. (2012) utilized the same method to search for variable X-ray sources in the 4 Ms CDF-S (Xue et al. 2011). They found 20 variable sources from 92 unclassified CDF-S X-ray sources using the probability threshold of $P_{X^2} < 0.05$. One of these 20 sources (XID 319) is actually a star, and it is correctly classified in Luo et al. (2017) based on its spectroscopy. Among the remaining 19 sources,[22] we confirm that eight sources[23] do have X-ray variability ($P_{X^2} < 0.015$). However, for the other 11 sources, our results show that when considering the 7 Ms CDF-S data, they do not satisfy the $P_{X^2} < 0.015$ or even the $P_{X^2} < 0.05$ threshold. We examine the light curves of the 11 sources and find the following two cases:

(1) If only the 4 Ms CDF-S data (i.e., the first four epochs of data) are considered, there are eight variable sources[24] whose P_{X^2} values meet the probability threshold of $P_{X^2} < 0.05$ used in Young et al. (2012). However, since the photon fluxes of these sources have hardly changed in subsequent epochs (5–7), when the 7 Ms CDF-S data (i.e., all seven epochs) are considered, the P_{X^2} values of these sources no longer meet the probability threshold requirement for selecting variable sources ($P_{X^2} < 0.05$). For example, Figure 2 displays the light curve of one of the sources, XID 920. The photon flux of this source exhibits significant fluctuation during the first four epochs (i.e., 4 Ms data; $P_{X^2,4\mathrm{Ms}} = 0.009$). However, in subsequent epochs (5–7), the photon flux of this source remains almost constant; the probability that its photon-flux fluctuation is produced by random fluctuation alone increases to $P_{X^2,7\mathrm{Ms}} = 0.052$, and it no longer satisfies the probability threshold requirement for selecting variable sources. There is a possibility that such sources are actually X-ray variable, but in the latest three epochs of observations, they do not display significant variability, due to relatively short time separations between the epochs, producing a larger P_{X^2} value than that from the 4 Ms data. For each of these eight sources, we perform simulations to estimate the probability that its variability cannot be detected with the 7 Ms data (i.e., $P_{X^2,7\mathrm{Ms}} > 0.05$), assuming that it is a variable source and its variability had been detected when considering the 4 Ms data (i.e., $P_{X^2,4\mathrm{Ms}} < 0.05$). The probabilities for the eight sources range between $\approx 28\%$ and 39% (see Section 5.1 for details). This result implies that two to three sources among the eight may possess X-ray variability, although their variability cannot be detected when considering the 7 Ms CDF-S data. For completeness, we list the eight

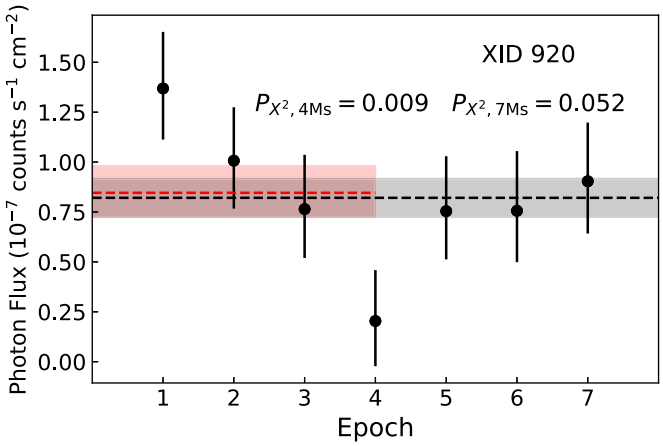

Figure 2. Light curve of XID 920. The black dashed line is the photon flux from the stacked 7 Ms (all seven epochs) data, and the gray shaded area represents its 1σ error. The red dashed line is the photon flux from the stacked 4 Ms (the first four epochs) data, and the red shaded area represents its 1σ error. The labels are XID, the $P_{X^2,4\mathrm{Ms}}$ value of the 4 Ms data, and the P_{X^2} value of the 7 Ms data. The photon flux of this source exhibits significant fluctuation during the first four epochs. However, in subsequent epochs (5–7), the photon flux of this source remains almost constant; the probability that the photon-flux fluctuation is produced by random noise alone increases and no longer meets the probability threshold requirement for selecting variable sources.

[22] The 19 sources are all unclassified in Luo et al. (2017).
[23] Their XIDs are 193, 282, 404, 558, 768, 813, 843, and 869.
[24] Their XIDs are 206, 298, 323, 349, 371, 565, 750, and 920.

Table 4
Properties of the Eight X-Ray Variable Candidates Selected Based on $P_{X^2,4Ms} < 0.05$

XID	z	Net counts	$\log L_{0.5-7keV,int}$ (erg s^{-1})	X^2_{4Ms}	$P_{X^2,4Ms}$	X^2_{7Ms}	$P_{X^2,7Ms}$	$\sigma^2_{NXS,corr}$	SFR ($M_\odot$ yr^{-1})	$\log M_\star$ ($M_\odot$)	Γ_{eff}
(1)	(2)	(3)	(4)	(5)	(6)	(7)	(8)	(9)	(10)	(11)	(12)
206	0.418	127.1	41.6	6.2	0.0312	9.5	0.1066	-0.01 ± 0.12	0.81	11.0	$1.07^{+0.33}_{-0.31}$
298	0.524	102.0	41.6	4.2	0.0411	5.4	0.4065	-0.11 ± 0.07	0.05	9.8	$1.28^{+0.34}_{-0.33}$
323	0.734	79.5	41.7	6.4	0.0111	9.8	0.0854	0.01 ± 0.05	0.25	11.7	$2.54^{+0.39}_{-0.43}$
349	0.964	207.4	42.4	9.2	0.0224	7.3	0.2331	-0.03 ± 0.04	0.47	11.4	$2.30^{+0.37}_{-0.37}$
371	0.679	30.1	41.1	5.0	0.0442	7.1	0.2098	0.01 ± 0.48	47.79	10.2	2.1
565	0.648	62.1	41.4	7.9	0.0131	7.8	0.1746	-0.08 ± 0.10	10.08	9.5	2.3
750	0.522	25.0	40.8	6.4	0.0483	8.6	0.1350	...	...	...	1.9
920	0.104	202.4	40.2	10.5	0.0090	11.5	0.0522	0.02 ± 0.09	...	...	$1.61^{+0.28}_{-0.27}$

Note. Column (5) and column (7) are the variability statistics from the first four and all seven epochs of data, respectively. Column (6) and column (8) are probabilities that the measured variability is due to Poisson noise alone considering the first four epochs of data and all seven epochs of data, respectively. The other columns have the same format as Table 2. XID 750 is included in the sample of Young et al. (2012), but it is not in our sample because it does not meet our sample selection criterion (less than 30 net counts in the full 7 Ms exposure). The measurements of the star formation rate and stellar mass are not available for XIDs 750 and 920. Statistically, five to six sources among the eight objects are expected to be false-positive detections. See Section 3.3 for details.

sources in Table 4 as possible candidates for being X-ray variable. Statistically, five to six of these sources are expected to be false-positive detections. We do not treat these objects as variable sources in the following analyses.

(2) For the other three sources (XIDs 149, 690, 916), their P_{X^2} values do not meet the probability threshold of $P_{X^2} < 0.05$ considering either the first four epochs of data or all seven epochs of data. The different results from Young et al. (2012) are mainly due to the differences in the extracted X-ray photometry. Compared to the 4 Ms survey, we detected fainter X-ray sources in the 7 Ms survey, which influences the estimated background levels, and for existing sources, we detected larger numbers of counts. These allow us to obtain more accurate source positions and photometric properties with the 7 Ms data.

In summary, among the 20 variable sources found in Young et al. (2012), XID 319 is actually a star, and 16 of the remaining 19 sources, using our extraction process, meet the selection criterion of variable sources ($P_{X^2} < 0.05$) used in Young et al. (2012) if considering the 4 Ms CDF-S data alone. However, only eight of the 16 sources satisfy the selection criterion of variable sources ($P_{X^2} < 0.05$) when using the 7 Ms CDF-S data.

Our analysis identifies five new variable sources (XIDs 231, 463, 545, 807, 808) relative to Young et al. (2012); the details of these sources are as follows:

XID 231: The source is not included in the sample of Young et al. (2012) because it does not have sufficient photons (less than 20 net counts in the first four epochs; see Young et al. 2012).

XID 545: The luminosity of the source is close to the boundary of AGN identification ($L_X > 3 \times 10^{42}$ erg s^{-1}), which causes this source to be classified into different types in the 4 Ms CDF-S and 7 Ms CDF-S (the source is classified as an AGN in the 4 Ms CDF-S; see Xue et al. 2011). Here, we find that this source exhibits significant X-ray variability, which is consistent with its identification in the 4 Ms CDF-S.

XIDs 463, 807: These two objects meet the selection criterion for variable sources ($P_{X^2} < 0.015$) considering either the first four epochs of data or all seven epochs of data. The different results from Young et al. (2012) are mainly due to the differences in the extracted X-ray photometry, and we expect that the photometric properties from the 7 Ms data are more accurate, as explained in point (2) above.

XID 808: The source does not meet the selection criterion of variable sources ($P_{X^2} < 0.05$) when considering the first four epochs of data. In the subsequent three epochs (5–7), however, the photon fluxes of this source show significant change. When considering all seven epochs of data, the source meets the selection criterion of variable sources ($P_{X^2} < 0.015$).

We also compare our selection to AGN candidates selected by optical variability in the CDF-S. Trevese et al. (2008) utilized optical variability (timescale of ~3 years) to search for AGN candidates in the AXAF field (~0.25 deg^2) that overlaps the CDF-S. They reported 132 optically variable AGN candidates, 39 of which fall into the field of view of the CDF-S. A total of 23 of the 39 sources have X-ray counterparts in the 7 Ms CDF-S main catalog using a matching radius of 0.″5. Among these 23 objects, 22 have been classified as AGNs in Luo et al. (2017), and only one source (XID 558) is unclassified. Our variability calculation suggests that XID 558 has significant X-ray variability, which is consistent with the result of Trevese et al. (2008) that XID 558 could be an AGN.

Villforth et al. (2010) utilized optical variability (timescale of ~3–6 months) to search for AGN candidates in the GOODS fields (~0.1 deg^2), and the GOODS-South field overlaps the CDF-S. They reported 139 optically variable AGN candidates, of which 40 high-significance (a significance level of 99.99%) candidates fall into the field of view of the CDF-S. A total of 19 of the 40 objects have X-ray counterparts in the 7 Ms CDF-S main catalog using a matching radius of 0.″5, of which 12 sources have been classified as AGNs in Luo et al. (2017) and seven sources are unclassified. Four (XIDs 446, 498, 553, and 558) of these seven unclassified sources are included in our sample (i.e., 110 unclassified X-ray sources). As mentioned above, XID 558 has significant X-ray variability. Our variability calculation suggests that XID 553 has lower-significance X-ray variability (see Table 3). XID 446 and 498 are not found to have X-ray variability, which is probably because (1) they have small numbers of net counts (XIDs 446 and 498 only have 45 and 32 total observed net counts, respectively), making their variability difficult to detect; or (2) they do not display X-ray variability during the CDF-S survey. Among the remaining 21 (40 – 19) candidates without X-ray

counterparts, 11 have off-axis angles of $<6'$ in the 7 Ms CDF-S, and they are not adjacent to any X-ray sources. We perform a stacking analysis for these 11 sources using the 7 Ms CDF-S data, and this sample does not show any stacked X-ray signal with a 3σ flux upper limit of 3.9×10^{-18} erg cm^{-2} s^{-1} in the 0.5–2 keV band (corresponding to a luminosity upper limit of 4.4×10^{39} erg s^{-1} at a mean redshift of 0.52). There are two possible interpretations regarding the nature of these objects: (1) they are not AGNs in general but are other kind of objects such as nuclear supernovae (e.g., Brandt 2005); (2) they are AGNs with small-scale X-ray absorbers that obscure X-ray emission but do not affect the observed optical emission (e.g., similar to the obscuring material in broad absorption line quasars).

Falocco et al. (2015) utilized optical variability (timescale of $\sim$1 year) to search for AGN candidates in the SUDARE-VOICE field ($\sim$2 deg^2) that covers the CDF-S. They reported 175 optically variable AGN candidates, only eight of which fall into the field of view of the CDF-S. Four of the eight sources have X-ray counterparts in the 7 Ms CDF-S main catalog with a matching radius of $0''.5$, and all four have been classified as AGNs in Luo et al. (2017).

4. LLAGN Candidates

There are three possible scenarios that may be responsible for the X-ray variability of the 13 variable sources, namely X-ray binary (XRB) populations, ultraluminous X-ray sources (ULXs), and accreting SMBHs. In this section, we investigate which scenario is the most probable case. For XID 869, its X-ray variability may be due to a ULX, while for the vast majority of the remaining 12 variable sources, their X-ray variability is most likely explained by the scenario of accreting SMBHs (i.e., AGNs).

4.1. Measuring Variability Amplitude

In order to analyze quantitatively the characteristics of variability, we adopt the normalized excess variance defined in Vaughan et al. (2003a):

$$\sigma_{\rm NXS}^2 = \frac{1}{(N-1)\langle {\rm PF}\rangle^2}\sum_{i=1}^{N}({\rm PF}_i - \langle {\rm PF}\rangle)^2 - \frac{1}{N\langle {\rm PF}\rangle^2}\sum_{i=1}^{N}(\delta {\rm PF}_i)^2. \quad (7)$$

The statistical uncertainty of $\sigma_{\rm NXS}^2$ is computed as $S_D/(\langle {\rm PF}\rangle^2\sqrt{N})$ (Vaughan et al. 2003a), where

$$S_D^2 = \frac{1}{N-1}\sum_{i=1}^{N}[({\rm PF}_i - \langle {\rm PF}\rangle)^2 - (\delta {\rm PF}_i)^2 - \sigma_{\rm NXS}^2\langle {\rm PF}\rangle^2]^2. \quad (8)$$

The normalized excess variance measures how strongly the photon-flux fluctuation of a source exceeds the expected measurement error. When photon-flux fluctuation is entirely consistent with noise rather than due to intrinsic source variability, the normalized excess variance is consistent with zero (i.e., $\sigma_{\rm NXS}^2 = 0$). Due to statistical fluctuations, the normalized excess variance may be negative. The normalized excess variance is calculated for an observed-frame energy band. For sources with different redshifts, their $\sigma_{\rm NXS}^2$ values actually reflect the variability amplitude of photon fluxes in different rest-frame energy bands. Nevertheless, there is evidence suggesting that the bandpass effects are small both for short-term and long-term variability of AGNs (e.g., Ponti et al. 2012; Yang et al. 2016; Zheng et al. 2017). Thus, we do not expect that the bandpass effects will materially affect our following analyses.

In practical measurements, the $\sigma_{\rm NXS}^2$ value will be affected by the sparse observing pattern of the CDF-S survey. Because the measured mean of the photon fluxes of a source (μ) reflects the mean of its sampled data points rather than the true mean of its photon fluxes (i.e., $\langle {\rm PF}\rangle$), the measured variance of its photon-flux fluctuation $\left(\sigma^2 = \frac{1}{N-1}\sum_{i=1}^{N}({\rm PF}_i - \mu)^2\right)$ is not the true variance (i.e., $\sigma_{\rm true}^2 = \frac{1}{N-1}\sum_{i=1}^{N}({\rm PF}_i - \langle {\rm PF}\rangle)^2$), and its σ^2 value (as well as $\sigma_{\rm NXS}^2$ value) will tend to be underestimated (e.g., Young et al. 2012; Allevato et al. 2013). Therefore, for each source, we apply a Monte Carlo simulation method to correct the measured mean (μ) of photon fluxes and the measured variance (σ^2) of photon-flux fluctuation, and then calculate the bias-corrected $\sigma_{\rm NXS}^2$ value ($\sigma_{\rm NXS,corr}^2$; e.g., Young et al. 2012). The specific procedure is described as follows.

We assume that all sources have intrinsic X-ray variability. For nonvariable sources, the measured variance of photon-flux fluctuation is regarded as an upper limit to the variability that could be present. We assume that the intrinsic X-ray variability of all sources can be simply described by a power-law power spectral density (PSD) function (i.e., $P(f) \propto f^{-\beta}$).[25] This PSD has usually been adopted in previous studies (e.g., Young et al. 2012; Allevato et al. 2013). Previous investigations of the long-term variability of nearby Seyfert galaxies found that $\beta \sim 1$ (e.g., Uttley et al. 2002; Vaughan & Fabian 2003; Vaughan et al. 2003b). However, recent studies reported that β may not be 1 and suggested $\beta = 1.2$–1.3 (e.g., Zheng et al. 2017). We adopt $\beta = 1$ and $\beta = 1.3$ to perform subsequent calculations. Following the procedure in Section 3 of Allevato et al. (2013), we take the measured mean (μ) and variance (σ^2) as "true" values to generate 5000 stochastic light curves based on the given power-law PSD, where each simulated light curve is generated five times longer than the sampled region in order to reproduce the effect of "red-noise leak." Each simulated light curve is resampled based on the actual observing pattern, and the sparsely sampled light curve is modified with Poisson noise to account for measurement errors. Finally, the mean ($\mu_{\rm sim}$) and variance ($\sigma_{\rm sim}^2$) of each simulated light curve are calculated, and the ratio of the "true" input value (i.e., the measured values used as input in the simulations) and the median of output values of all simulated light curves (i.e., the biased values produced by sparse sampling) is computed as

$$f_{\rm mean} = \mu/{\rm median}(\mu_{\rm sim}), \quad (9)$$

$$f_{\rm variance} = \sigma/{\rm median}(\sigma_{\rm sim}), \quad (10)$$

where $f_{\rm mean}$ is the rescaling factor of the mean and $f_{\rm variance}$ is the rescaling factor of the variance. For our full sample (505 sources), the values of $f_{\rm mean}$ are in the range $\approx$0.6–1.2, with a median value of $\approx$0.9. The values of $f_{\rm variance}$ vary between

[25] We compare the $\sigma_{\rm NXS,corr}^2$ values calculated using this simple power-law PSD function to those calculated using a more complicated PSD function described in Section 5.4. We find that the differences between the $\sigma_{\rm NXS,corr}^2$ values calculated using these two different PSD functions are small, far less than the typical uncertainty of $\sigma_{\rm NXS,corr}^2$. Therefore, for simplicity, this simple power-law PSD function is used in the calculations of $\sigma_{\rm NXS,corr}^2$.

≈0.5 and 2.7, with a median value of ≈1.2. For 69% of the sources, their $f_{\rm variance}$ values are larger than one, indicating that their variances are underestimated because of the sampling bias. Using the rescaling factors, the biased measured mean (μ) and variance (σ^2) can be corrected (i.e., $\langle {\rm PF} \rangle = f_{\rm mean} \times \mu$; $\sigma_{\rm true} = f_{\rm variance} \times \sigma$), and then the bias-corrected $\sigma^2_{\rm NXS}$ value ($\sigma^2_{\rm NXS,corr}$) and its statistical uncertainty (err($\sigma^2_{\rm NXS,corr}$)) are calculated using Equations (7)–(8).

We perform the above procedure to calculate the $\sigma^2_{\rm NXS,corr}$ value of each source in our full sample (505 sources). The influence of different β values adopted (i.e., $\beta = 1$ and $\beta = 1.3$) on the calculated results of $\sigma^2_{\rm NXS,corr}$ is small, with an average relative deviation of ∼3.2%. This difference is much smaller than the statistical uncertainty of $\sigma^2_{\rm NXS,corr}$ itself. Thus, for simplicity, we only use $\sigma^2_{\rm NXS,corr}$ values calculated with $\beta = 1$ in the following analyses. The $\sigma^2_{\rm NXS,corr}$ values and their 1σ uncertainties for the 13 variable sources are listed in Table 2, where the $\sigma^2_{\rm NXS,corr}$ values of two variable sources (XID 807 and XID 808) are completely dominated by statistical uncertainty (i.e., $\sigma^2_{\rm NXS,corr} \leqslant {\rm err}(\sigma^2_{\rm NXS,corr})$). Even though we correct the bias produced by sparse sampling, an individual $\sigma^2_{\rm NXS,corr}$ value may still be highly uncertain, as shown in Allevato et al. (2013). Thus the $\sigma^2_{\rm NXS,corr}$ values are best considered in the ensemble of a specific group rather than on the basis of an individual object.

4.2. The Scenario of an XRB Population

Discrete XRBs are the main contributors of galaxy-wide X-ray luminosity for normal galaxies. To diagnose whether XRB populations can be responsible for the X-ray variability of these variable sources, below we compare the measured intrinsic X-ray luminosity ($L_{2-10\,{\rm keV,int}}$) and variability amplitude of each of the 13 variable sources to those expected from XRB populations.

The potential galaxy-wide X-ray luminosity from XRB populations ($L_{2-10\,{\rm keV,XRB}}$) is composed of luminosities of low-mass X-ray binaries (LMXBs) and high-mass X-ray binaries (HMXBs). Previous studies have demonstrated that the total X-ray luminosities from the LMXB population and HMXB population are proportional to the stellar mass ($M_\star$) and star formation rate (SFR) of the host galaxy, respectively (e.g., Gilfanov 2004; Gilfanov et al. 2004a; Lehmer et al. 2010, 2016). Lehmer et al. (2016) provided the following redshift-dependent empirical relation:

$$\begin{aligned} L_{2-10\,{\rm keV,XRB}} &= L_{\rm LMXB} + L_{\rm HMXB} \\ &= \alpha(1+z)^{\gamma} M_\star + \beta(1+z)^{\delta} {\rm SFR}, \end{aligned} \quad (11)$$

where $\log \alpha = 29.30$, $\log \beta = 39.40$, $\gamma = 2.19$, and $\delta = 1.02$, which are the best-fit values from the 6 Ms CDF-S data.

We collect the values of $M_\star$ and SFR of each source in our full sample (505 sources) by cross-matching the optical counterpart position of each source to the CANDELS catalog (Santini et al. 2015) with a matching radius of $0\farcs5$. The CANDELS catalog provides multiple estimated values of $M_\star$ and SFR that were calculated by different teams through spectral energy distribution (SED) fittings. Following Yang et al. (2017), we adopt the median values of $M_\star$ and SFR from five teams (labeled as $2a_\tau$, $6a_\tau$, $11a_\tau$, $13a_\tau$, and $14a$ in Santini et al. 2015). The five teams adopted the same stellar templates from Bruzual & Charlot (2003) and the Chabrier IMF when performing the SED fittings. Excluding 41 sources that have different redshifts in the CANDELS catalog and the 7 Ms CDF-S catalog ($|\Delta z|/(1+z_{\rm CANDELS}) > 0.15$), we obtain the $M_\star$ and SFR values for 83 nonvariable, unclassified X-ray sources, 269 AGNs, and the 13 variable sources. The values of $M_\star$ and SFR for the 13 variable sources are listed in Table 2. Since the empirical relation of Lehmer et al. (2016) was obtained under the assumption of the Kroupa (2001) IMF, in the calculations of $L_{2-10\,{\rm keV,XRB}}$ using Equation (11), we correct the values of $M_\star$ and SFR from the Chabrier IMF to the Kroupa IMF following the prescription of Madau & Dickinson (2014). The measured 0.5–7 keV intrinsic X-ray luminosity ($L_{0.5-7{\rm keV,int}}$) and effective photon index ($\Gamma_{\rm eff}$) of each source are provided in Luo et al. (2017). Based on the effective photon index of each source, the 2–10 keV intrinsic X-ray luminosity ($L_{2-10,{\rm keV,int}}$) is converted from $L_{0.5-7{\rm keV,int}}$.

Figure 3 presents the measured 2–10 keV intrinsic luminosities versus those expected from XRB populations for the 13 variable sources (red solid stars). The black dashed line indicates the unity relation, while the gray shaded area represents the expected 1σ dispersion of the derived $L_{2-10\,{\rm keV,XRB}}$ values (0.17 dex; Lehmer et al. 2016). Except for two variable objects (XIDs 193 and 558), the measured luminosities of the remaining variable sources are higher than those expected from XRB populations. For reference, the data points of the 83 nonvariable, unclassified X-ray sources with available SFR and $M_\star$ measurements are also shown in Figure 3 (blue solid circles), which also generally lie above the unity line. Equation (11) was obtained from stacked samples of normal galaxies in the CDF-S, where most of the galaxies are not detected in the X-ray band (Lehmer et al. 2016). We also expect strong intrinsic scatter in this empirical relation. Therefore, it is perhaps not surprising to observe that X-ray-detected galaxies in the CDF-S, whether variable or nonvariable, tend to reside in the bright end of the scatter and lie above the unity relation in Figure 3. Thus this comparison cannot rule out the possibility that the X-ray emissions of the 13 variable sources are produced by XRB populations.

We then compare the measured variability amplitude to that expected from XRB populations following an approach similar to that in Section 4.2 of Young et al. (2012). To examine the potential contributions of XRB populations to variability, we first determine the relative contributions of HMXBs and LMXBs for each source. We calculate the expected X-ray luminosities from HMXBs ($L_{\rm HMXB}$) and LMXBs ($L_{\rm LMXB}$). Then, according to the ratio of $L_{\rm LMXB}/L_{\rm HMXB}$, the 13 variable sources are divided into two classes. One class is expected to have the X-ray luminosities dominated by HMXBs, and the other class is expected to have the X-ray luminosities dominated by LMXBs. There are only two variable sources (XIDs 807 and 843) whose expected X-ray luminosities are dominated by LMXBs. Based on the "universal" HMXB (LMXB) X-ray luminosity function, Gilfanov et al. (2004b) used Monte Carlo simulations to obtain a theoretical relation between $\sigma_{\rm rms,tot}/\sigma_{\rm rms,0}$ and SFR ($M_\star$) for the HMXB (LMXB) population, where $\sigma_{\rm rms,tot}$ is the square root of normalized excess variance of the whole HMXB (LMXB) population and $\sigma_{\rm rms,0}$ is the square root of normalized excess variance of an individual XRB, which can be as large as 20%–30% on one-year timescales (e.g., Gilfanov 2010). We adopt $\sigma_{\rm rms,0} = 30\%$ to obtain the upper limit on $\sigma^2_{\rm rms,tot}$ as a function of SFR ($M_\star$) in the case of an HMXB (LMXB) dominant population.

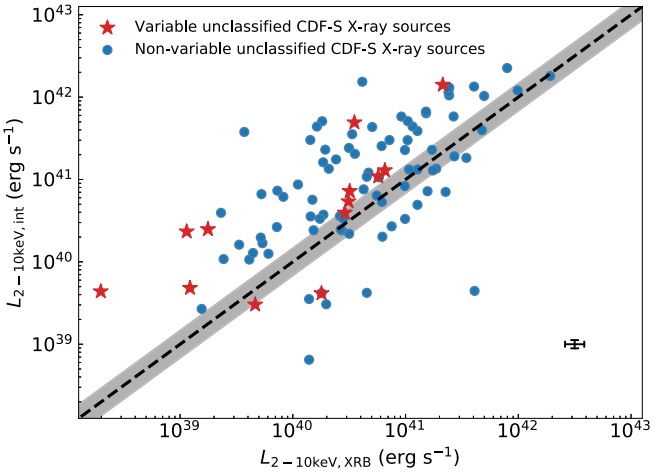

Figure 3. Observed 2–10 keV X-ray luminosity ($L_{2-10,\mathrm{keV,int}}$) vs. that expected from XRB populations ($L_{2-10\ \mathrm{keV,XRB}}$) for the 13 variable CDF-S X-ray sources (red solid stars). The data points of the 83 nonvariable unclassified X-ray sources with available SFR and $M_\star$ measurements (blue solid circles) are plotted for reference. The black dashed line is $L_{2-10\ \mathrm{keV,int}} = L_{2-10\ \mathrm{keV,XRB}}$, and the gray shaded area shows the expected 1σ dispersion of the derived $L_{2-10\ \mathrm{keV,XRB}}$ (0.17 dex; Lehmer et al. 2016). The black cross in the lower right corner represents the average error bar of the data points.

Figure 4 displays SFR ($M_\star$) versus $\sigma^2_{\mathrm{NXS,corr}}$ for the HMXB-dominated (LMXB-dominated) variable sources (red stars), and the predicted upper limit on $\sigma^2_{\mathrm{rms,tot}}$ in the case of the HMXB (LMXB) dominant population is also shown (black solid curve). For reference, the data points of the 83 nonvariable, unclassified X-ray sources with available SFR and $M_\star$ measurements are also included in this figure (blue solid circles), where 76 nonvariable, unclassified X-ray sources with negative $\sigma^2_{\mathrm{NXS,corr}}$ values are placed at the 10^{-3} level and marked by the arrows. The variability amplitudes of the 13 variable sources are significantly higher than the upper limit of variability amplitude expected from XRB populations. This result indicates that the X-ray variability of the 13 variable sources is unlikely to be caused by XRB populations.

4.3. The Scenario of ULXs

ULXs are another potential explanation for the X-ray variability of our selected variable sources. ULXs are defined as nonnuclear, point-like objects that have been observed at least once at an apparent isotropic X-ray luminosity higher than those of stellar-mass black holes (Feng & Soria 2011; Kaaret et al. 2017). The typical X-ray luminosity range of ULXs is 10^{39}–10^{41} erg s^{-1} (Lehmer et al. 2006). However, for the ULXs found in early-type galaxies, they often have lower luminosities, with $L_{0.5-8\mathrm{keV,int}} < 2 \times 10^{39}$ erg s^{-1} (Swartz et al. 2004).

One method of identifying ULXs is to search for off-nuclear X-ray sources (see Hornschemeier et al. 2004; Lehmer et al. 2006; Mainieri et al. 2010). Figure 5 presents postage-stamp images ($4'' \times 4''$) of *HST* F606W from GOODS-S (Giavalisco et al. 2004) or F125W from CANDELS (Grogin et al. 2011; Koekemoer et al. 2011) for the 13 variable sources. The red and gray circles overplotted on each image are the positional uncertainties of the X-ray source ($\triangle_X$) and the TENIS K_s-band counterpart ($\triangle_{K_s}$[26]) at 90% confidence levels, respectively. As in Lehmer et al. (2006), we consider that an X-ray source is off-nuclear if its X-ray positional offset from the galactic nucleus is larger than the total positional uncertainty ($\triangle = \sqrt{\triangle_X^2 + \triangle_{K_s}^2}$), where the position of the TENIS K_s-band counterpart is considered as the position of the galactic nucleus (the K_s-band data suffer less from dust obscuration or confusion from young star-forming regions). According to this criterion, there is one off-nuclear variable source, XID 869. For this source, the offset angle between its X-ray position and its galactic nucleus is $1\farcs1$, and the confidence level of its X-ray position deviating from its galactic nucleus is ≈98.8%. Since we searched for off-nuclear X-ray sources 13 times, we conservatively estimate that the probability of the deviation being caused by chance is ≈15.6% (i.e., $13 \times 1.2\%$) after applying the Bonferroni correction.[27] Therefore, the positional offset is likely intrinsic, and XID 869 could be a ULX. It also has a low X-ray luminosity, with $L_{0.5-8\mathrm{keV,int}} \approx 5 \times 10^{39}$ erg s^{-1}, which is consistent with the typical X-ray luminosities of ULXs.[28]

Five variable sources (XIDs 282, 463, 545, 808, 813) have luminosities that are larger than the typical luminosities of ULXs (i.e., $L_{0.5-8\mathrm{keV,int}} > 10^{41}$ erg s^{-1}), which suggests they are likely not ULXs. Seven variable sources have luminosities ($L_{0.5-8\mathrm{keV,int}}$) less than 10^{41} erg s^{-1}. For four variable sources (XIDs 231, 404, 807, 843) whose luminosities are in the range of 10^{40}–10^{41} erg s^{-1}, their host galaxy morphologies are all early-type (see Figure 5). Their higher X-ray luminosities (relative to 2×10^{39} erg s^{-1}, the typical luminosity upper limit of ULXs found in early-type galaxies; e.g., Swartz et al. 2004) suggest that they are likely not ULXs. For the remaining three variable sources (XIDs 193, 558, 768) in the luminosity range 10^{39}–10^{40} erg s^{-1}, their variability being due to a ULX near the galactic nucleus cannot be ruled out. Nevertheless, XID 558 and an unclassified, nonvariable off-nuclear X-ray source XID 556 are a pair of X-ray sources and have strong radio emission (see Luo et al. 2017). They could be the radio core plus extended radio jet/lobe of a radio-loud AGN and are unlikely to be a pair of ULXs with radio emission. In addition, XID 558 also displays optical variability (see Section 3.3). Thus, XID 558 can be considered as a good AGN candidate.

4.4. AGN Candidates and Their Basic Properties

Through the above analyses, we find that for nine variable sources with luminosities ($L_{0.5-8\mathrm{keV,int}}$) greater than 10^{40} erg s^{-1}, their X-ray variability is most likely attributed to the scenario of accreting SMBHs (i.e., AGNs). They are good AGN candidates. Among the four variable sources (XIDs 193, 558, 768, 869) with luminosities ($L_{0.5-8\mathrm{keV,int}}$) less than 10^{40} erg s^{-1}, XID 869 is an off-nuclear source and could be a ULX. XID 558 can be considered as a good AGN candidate (see Section 4.3). XID 193 and XID 768 are considered as AGN candidates in the following analyses, but we caution that the possibility that they are ULXs near the galactic nucleus cannot be excluded based on the current information. In summary, except for one variable source XID 869, which could be a ULX, we find 12 AGN candidates, of which 11 are LLAGN candidates ($L_{0.5-7\mathrm{keV,int}} < 10^{42}$ erg s^{-1}). Below we report the basic properties of the 12 AGN candidates. The remaining 97 nonvariable, unclassified X-ray sources and the

[26] Following Luo et al. (2017), we adopt $0\farcs1$ as the 1σ positional uncertainty of the TENIS K_s-band counterpart, so $\triangle_{K_s} \approx 0\farcs16$ in here.

[27] https://en.wikipedia.org/wiki/Bonferroni_correction

[28] The 0.5–8 keV intrinsic X-ray luminosity ($L_{0.5-8\mathrm{keV,int}}$) is converted from $L_{0.5-7\mathrm{keV,int}}$ based on the effective photon index.

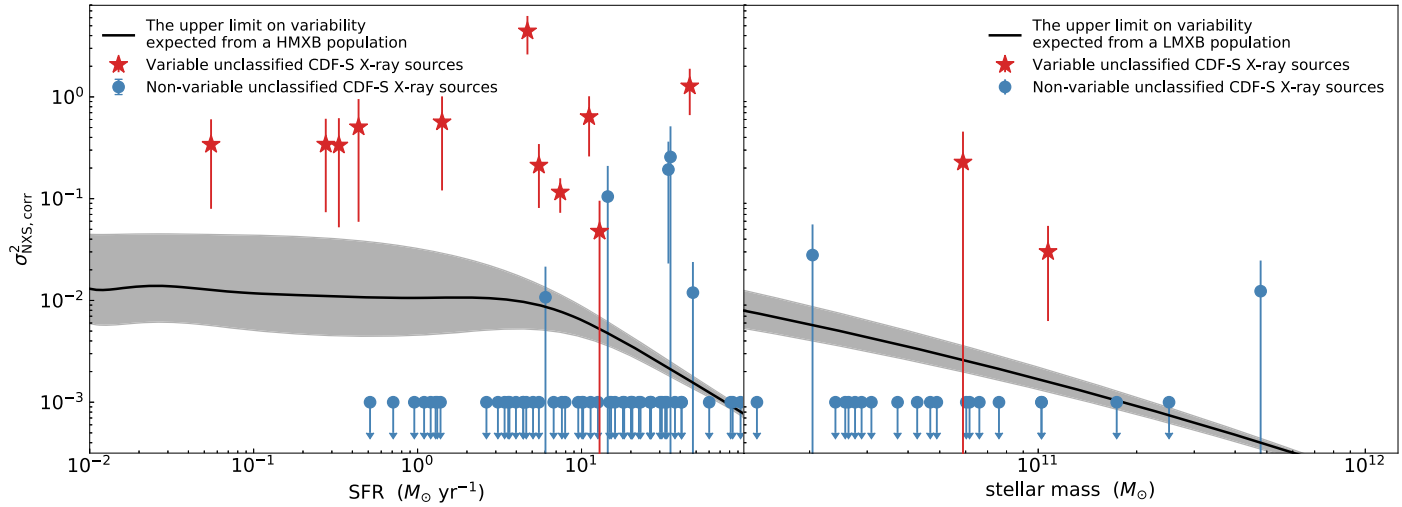

Figure 4. Left panel: $\sigma^2_{\rm NXS,corr}$ vs. SFR for the 11 variable CDF-S X-ray sources (red solid stars) whose X-ray luminosities are dominated by an HMXB population. Right panel: $\sigma^2_{\rm NXS,corr}$ and $M_\star$ for the two variable CDF-S X-ray sources (XIDs 807 and 843; red solid stars) whose X-ray luminosities are dominated by an LMXB population. The black solid curve in the left (right) panel is the upper limit on $\sigma^2_{\rm rms,tot}$ as a function of SFR ($M_\star$) in the case of an HMXB (LMXB) dominant population when adopting $\sigma_{\rm rms,0} = 30\%$. The shaded areas represent the 1σ dispersion derived from the simulations of Gilfanov et al. (2004b). The data points of the 83 nonvariable, unclassified X-ray sources with available SFR and $M_\star$ measurements (blue solid circles) are also included for reference, where 76 sources with negative $\sigma^2_{\rm NXS,corr}$ values are placed at the 10^{-3} level and marked by the arrows. The variability amplitudes of the 13 variable sources are significantly higher than the upper limit of variability amplitude expected from XRB populations, which suggest that the variability of these variable sources is likely not caused by XRB populations.

ULX XID 869 are treated as normal galaxies in the following analyses.

The 12 AGN candidates all have optical spectroscopic observations (Szokoly et al. 2004; Mignoli et al. 2005; Balestra et al. 2010; Silverman et al. 2010; Kurk et al. 2013), with spectroscopic redshifts ranging from 0.07 to 0.83. The optical spectra of the 12 AGN candidates reveal only narrow emission lines or absorption lines. Four sources (XIDs 282, 404, 558, 813) are classified by Szokoly et al. (2004) in more detail. XID 404 has a sufficiently large signal-to-noise ratio in the optical spectrum for line ratio measurement, and it is classified as a low-ionization nuclear emission-line region based on the line ratio diagnostics. The other three sources are classified as having unresolved emission lines consistent with a H II region-type spectrum.

Figure 6 presents the intrinsic 0.5–7 keV luminosity versus redshift (left panel) and the luminosity distribution (right panel) for the 12 variability-selected AGN candidates. For comparison, the intrinsic 0.5–7 keV luminosity versus redshift for the 98 normal galaxies (97 nonvariable, unclassified X-ray sources and one ULX XID 869) and 103 AGNs with $L_{0.5-7{\rm keV,int}} < 3 \times 10^{42}$ erg s^{-1} in our AGN sample (i.e., 395 AGNs) are also included. The 103 AGNs do not meet the luminosity criterion for selecting AGNs; they are selected by other criteria (see Luo et al. 2017 for details). Of the 103 AGNs, only 14 are classified as such using optical spectra. The median luminosity of the 12 variability-selected AGN candidates is significantly smaller than that of the 103 AGNs. A Kolmogorov–Smirnov (K-S) test demonstrates that there is a significant difference between the luminosities of the 12 variability-selected AGN candidates and the 103 AGNs ($p = 8 \times 10^{-5}$). This result indicates that the X-ray variability selection technique can effectively identify AGNs with low intrinsic X-ray luminosity (especially for $L_{0.5-7{\rm keV,int}} < 10^{41}$ erg s^{-1}) compared with other selection criteria.

The effective power-law photon indices ($\Gamma_{\rm eff}$) of the 12 AGN candidates were calculated in Luo et al. (2017) from the hard-to-soft band ratios by assuming that the 0.5–7 keV spectra are power laws modified by only Galactic absorption. For the 12 AGN candidates, six sources are only detected in the soft band or the hard band. For these sources, the best-guess values of band ratios were estimated by using the Bayesian code BEHR (Park et al. 2006). The effective power-law photon indices of the 12 AGN candidates are listed in Table 2, and the average effective power-law photon index is 1.82.

We also use XSPEC 12.9 (Arnaud 1996) to fit the 0.5–7 keV spectra of the 12 AGN candidates. The C statistic (Cash 1979) is employed to determine the best fit in the fittings. For five AGN candidates with numbers of net counts higher than 100, we fit their spectra individually. We use a power-law model modified by Galactic absorption (WABS*ZPOWERLW) to fit their spectra; an intrinsic absorption component is not required in all cases as it does not improve the fits. The fitting results for the five sources are listed in Table 5. Their $\Gamma_{\rm XSPEC}$ values are in general consistent with the $\Gamma_{\rm eff}$ values given in Luo et al. (2017). XID 545 has a hard photon index compared to ordinary AGNs, which may be caused by some intrinsic absorption that cannot be constrained by the current limited data. For the remaining seven sources, we use a power-law model modified by Galactic absorption with the same photon index to jointly fit their spectra. The best-fit photon index is $2.07^{+0.19}_{-0.18}$. This soft photon index indicates that the seven sources are, on average, not obscured.

Two (XID 193 and XID 558) of the 12 AGN candidates (~16%) are detected at 1.4 GHz by the VLA (see 7 Ms CDF-S main catalog in Luo et al. 2017). Their radio-loudness parameters, $R_{\rm L} = f_\nu(5\,{\rm GHz})/f_\nu(4400\,{\rm \AA})$, are calculated following Kellermann et al. (1989). We convert $f_\nu(1.4\,{\rm GHz})$ to $f_\nu(5\,{\rm GHz})$ by assuming that the radio SED has a shape of $f_\nu \propto \nu^{-0.8}$. We estimate $f_\nu(4400\,{\rm \AA})$ from the intrinsic X-ray luminosity of each source according to the average SED of

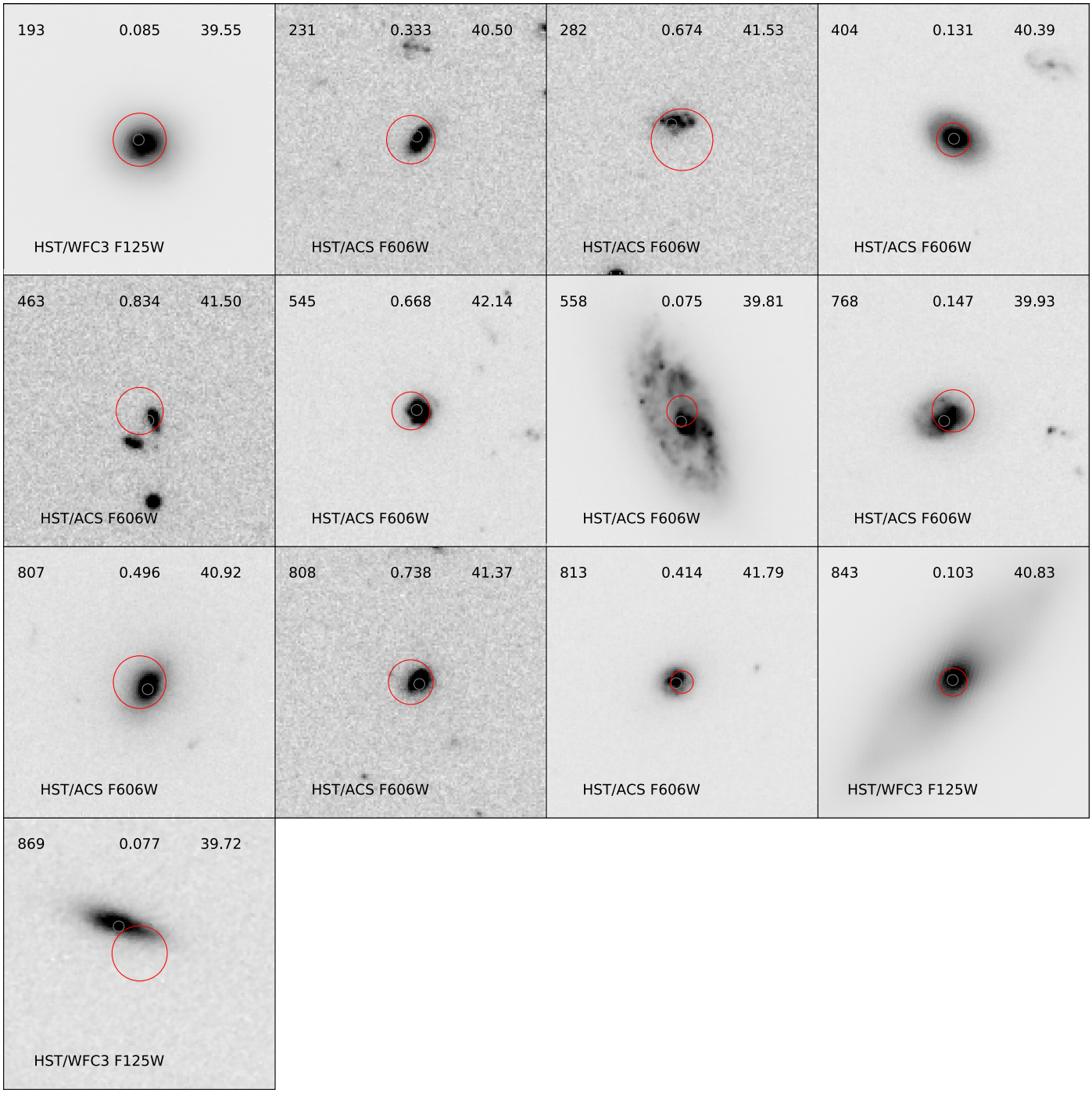

Figure 5. Postage-stamp images in the GOODS-S/F606W (or CANDELS/F125W) band for the 13 variable sources. Each image is $4'' \times 4''$ with the position of the X-ray source of interest located at the center. The label at the top of each image gives the XID, redshift, and logarithm of the intrinsic rest-frame 0.5–8 keV luminosity, from left to right. The red and gray circles overplotted on each image are the positional uncertainties of the X-ray source and the TENIS K_s-band counterpart at 90% significance levels, respectively.

AGNs; the observed optical flux is not adopted here because it is significantly contaminated by host galaxy starlight, which will severely bias the computed R_L value (e.g., Padovani 2017). We adopt the average SED of type 1 quasars given by Richards et al. (2006) and the average SED of AGNs with low accretion rates ($\lambda_{Edd} < 10^{-3}$) given by Ho (2008) to estimate f_ν(4400 Å). In the former case, the radio-loudness parameters of XID 193 and XID 558 are ∼100 and ∼218, respectively. In the latter SED template, the radio-loudness parameters are ∼990 and ∼1800, respectively. The results in both cases suggest that the two LLAGN candidates can be classified as radio-loud AGNs and may have strong relativistic jets.

We also investigate the host-galaxy properties for the 12 variability-selected AGN candidates. The distribution of SFR versus $M_\star$ for the 12 host galaxies is shown in Figure 7. For comparison, the data points of 28 LLAGNs ($L_{0.5-7keV,int} < 10^{42}$ erg s^{-1}) and 53 higher-luminosity AGNs ($L_{0.5-7keV,int} > 10^{42}$ erg s^{-1}) in our AGN sample (i.e., 395 AGNs), and 75 normal galaxies (74 nonvariable, unclassified X-ray sources and one ULX XID 869), having $z < 1$ and available SFR and

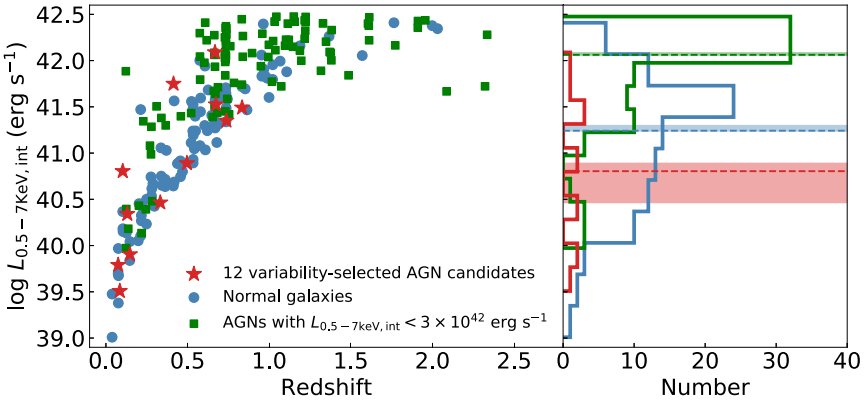

Figure 6. Left panel: intrinsic 0.5–7 keV luminosity vs. redshift distribution for the 12 variability-selected AGN candidates (red stars). The data points of the 98 normal galaxies (97 nonvariable, unclassified X-ray sources and one ULX XID 869; blue solid circles) and 103 AGNs with $L_{0.5-7\mathrm{keV,int}} < 3\times10^{42}$ erg s^{-1} (green solid squares) in our AGN sample are included for comparison. Right panel: distribution of luminosities for the corresponding samples. The dashed lines are the median values of luminosities for the corresponding samples, and the shaded areas show 1σ uncertainties on the median luminosities, which are calculated from 10,000 bootstrap samplings.

Table 5
X-Ray Spectral Fitting Results of Five Variability-selected AGN Candidates with Numbers of Net Counts Higher than 100

XID	Γ_{XSPEC}	Flux (10^{-16} erg cm^{-2} s^{-1})
(1)	(2)	(3)
404	$1.51^{+0.20}_{-0.19}$	2.99
545	$1.14^{+0.29}_{-0.28}$	4.60
558	$1.95^{+0.40}_{-0.34}$	4.14
813	$1.60^{+0.16}_{-0.16}$	6.8
843	$1.98^{+0.14}_{-0.13}$	19.9

Note. Columns: (1) Sequence number. (2) Best-fit power-law photon index obtained from spectral fitting and its 1σ lower and upper uncertainties. (3) Galactic absorption-corrected flux in the full band (0.5–7 keV).

$M_\star$ measurements, are also included in this figure. The dashed line and solid line show the star-forming main sequences at $z\sim0$ and $z\sim1$, respectively (Elbaz et al. 2007). For the 12 AGN candidates ($0<z<1$), 10 of 12 are located above the star-forming main sequence at $z\sim0$ (seven of 12 above the star-forming main sequence at $z\sim1$), indicating that they tend to inhabit star-forming galaxies. The stellar mass distribution of their host galaxies is not significantly different from that of the 28 LLAGNs (K-S test $p=0.72$) selected by the other criteria in Luo et al. (2017) or the 75 normal galaxies ($p=0.22$), but it is significantly different from that of the 53 higher-luminosity AGNs ($p=7\times10^{-4}$). Most (~72%) of the 53 higher-luminosity AGNs reside in high-mass galaxies ($\log M_\star > 10.3$). For the 28 LLAGNs plus 11 LLAGN candidates, ~31% of the sources inhabit high-mass galaxies ($\log M_\star > 10.3$), and ~44% of the sources reside in low-mass dwarf galaxies ($\log M_\star < 9.5$). The sources hosted in high-mass galaxies likely have black hole masses comparable to those of the higher-luminosity AGNs, and their low X-ray luminosities are probably attributed to inefficient accreting. Conversely, those sources inhabiting low-mass dwarf galaxies may be lower-mass black holes with typical accretion rates, similar to the low-luminosity quasars reported in Laha et al. (2018). In terms of the star formation rates of host galaxies, the distributions of the four samples (i.e., 12 AGN candidates, 28 LLAGNs, 53 higher-luminosity AGNs, and 75 normal galaxies) are not significantly different from each other.

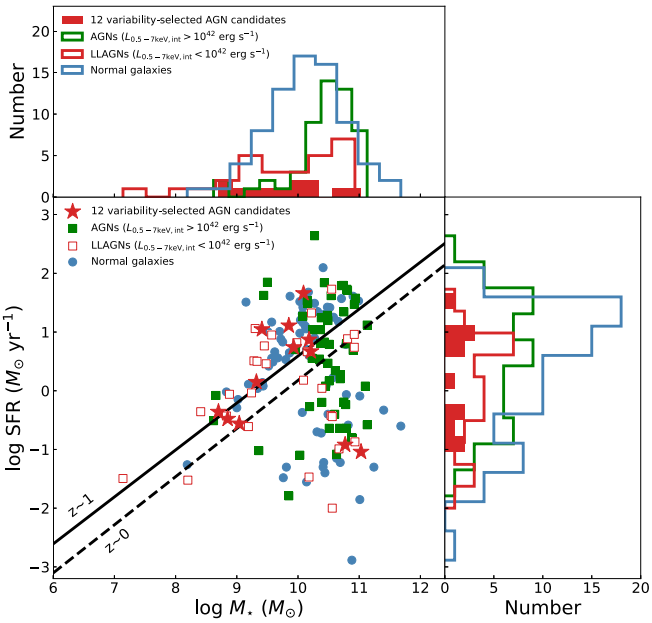

Figure 7. Distribution of star formation rate vs. stellar mass ($M_\star$) for the 12 variability-selected AGN candidates (red stars). For comparison, the data points of 28 LLAGNs ($L_{0.5-7\mathrm{keV,int}} < 10^{42}$ erg s^{-1}; red open squares), 53 higher-luminosity AGNs ($L_{0.5-7\mathrm{keV,int}} > 10^{42}$ erg s^{-1}; green solid squares), and 75 normal galaxies (74 nonvariable, unclassified X-ray sources and one ULX XID 869; blue solid circles), having $z<1$ and available SFR and $M_\star$ measurements, are plotted. The dashed line and solid line show the star-forming main sequences at $z\sim0$ and $z\sim1$, respectively (Elbaz et al. 2007).

5. Discussion

5.1. Efficiency of X-Ray Variability Selection of LLAGNs

As shown in Section 4.4, using the X-ray variability selection technique, we can identify LLAGN candidates that are usually missed by other selection methods and have low intrinsic X-ray luminosity ($L_{0.5-7\mathrm{keV,int}} < 10^{41}$ erg s^{-1}). However, the efficiency of X-ray variability selection of AGNs is critically dependent on the ability to detect X-ray variability. Generally, whether the variability of a source can be detected is related to the number of its observed net counts and its own variability amplitude given a fixed sampling pattern. We perform simulations to estimate the efficiency of detecting X-ray-variable AGNs given different total numbers of observed

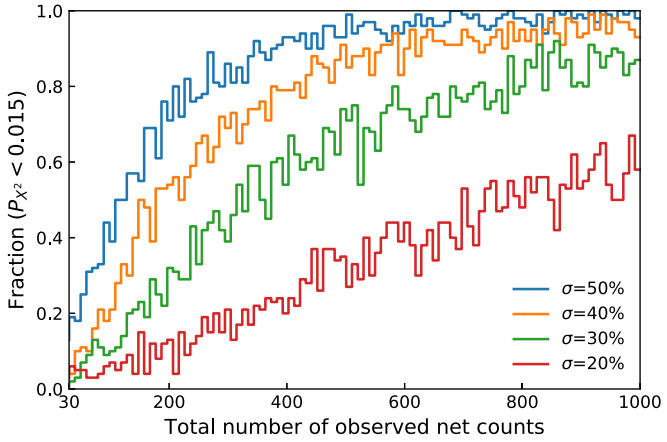

Figure 8. Fractions of simulated light curves that have detectable variability vs. the total number of observed net counts. Four sets of fractions are presented under the assumption that the AGN variability amplitude is $\sigma = 20\%$, 30%, 40%, and 50%.

net counts and variability amplitude. The specific procedure is described as follows.

We choose a source from 407 sources (12 variability-selected AGN candidates and 395 AGNs) and then rescale the number of its observed net counts and variability amplitude (i.e., the variance of its photon-flux fluctuation σ^2) to different values, where the number of observed net counts is rescaled by uniformly increasing the exposure time of each observation in each epoch so that the photon fluxes of the source do not change. In each realization, we generate 1000 simulated light curves based on the method described in Section 4.1, and we then calculate the P_{X^2} value of each simulated light curve using the method described in Section 3.1. In this process, each simulated light curve is sampled based on the sparse observing pattern of the CDF-S survey and divided into seven epochs (i.e., Table 1). Using $P_{X^2} < 0.015$ as the threshold criterion for selecting variability, we obtain the fraction of simulated light curves that have detectable variability; the fraction reflects the ability to detect variability (i.e., the possibility that the variability of an AGN can be detected) under given conditions. We repeat this process for all 407 sources to obtain an average result.

The fractions as a function of the number of net counts are presented in Figure 8, which displays four sets of fractions under the rescaling of the AGN variability amplitude to $\sigma = 20\%$, 30%, 40%, and 50%. As expected, the ability to detect variability increases with the increase in the total number of net counts and the variability amplitude of a source. When the total number of observed net counts is less than 100, even if the variability amplitude of the source is $\sigma = 50\%$ (above the average level of variability amplitude of AGNs, ∼30%–40%, e.g., Paolillo et al. 2004, 2017), the probability that this level of variability can be detected is only ∼50%. This result strongly suggests that the 12 variability-selected AGN candidates are probably only the "tip of the iceberg" of unidentified LLAGNs, and some unclassified CDF-S X-ray sources may still host LLAGNs but do not exhibit detectable variability because of the small number of net counts measured.[29] It is likely not feasible to identify variable LLAGNs by combining the sample objects into a group to increase the total number of net counts and searching collective variability, because (1) individual LLAGNs in the group will likely not vary coordinately, which will reduce the amplitude of the collective variability, and (2) nonvariable normal galaxies in the group will dilute the amplitude of the collective variability (see Equation (7)).

The simulation results indicate that in the low-count regime, we tend to detect X-ray variability for sources with large variability. This variability-detection bias will lead to an overestimation of the measured overall variability amplitude of AGNs in the low-count regime, due to the absence of some of the AGNs that have weak and undetectable variability, as also suggested by previous studies (e.g., Allevato et al. 2013; Paolillo et al. 2017). In addition, the simulations demonstrate that when the total number of observed net counts is higher than 500 for AGNs with an average level of variability amplitude ($\sigma \approx 30\%$–40%), the probability of detecting their variability is ≈60%–80%.

In the above simulation, the $P_{X^2,4\mathrm{Ms}}$ and $P_{X^2,7\mathrm{Ms}}$ values for each simulated light curve can be calculated. Based on these two values for the 1000 simulated light curves, we can compute the proportion of the number of simulated light curves with $P_{X^2,4\mathrm{Ms}} < 0.05$ and $P_{X^2,7\mathrm{Ms}} > 0.05$ to the number of simulated light curves with $P_{X^2,4\mathrm{Ms}} < 0.05$. This proportion reflects the probability that the variability of a variable source cannot be detected when considering the 7 Ms data ($P_{X^2,7\mathrm{Ms}} > 0.05$) on the premise that its variability has been detected with the 4 Ms data ($P_{X^2,4\mathrm{Ms}} < 0.05$). We calculate this probability for each of the eight variable sources mentioned in Section 3.3 and find that the probabilities range between ≈28% and 39%.

5.2. Fraction of Variable AGNs

We investigate the fractions of variable AGNs in different luminosity bins. Using the method described in Section 3.1 ($P_{X^2} < 0.015$ as threshold criterion for selecting variability), we find 136 variable AGNs among the 395 AGNs. Figure 9 presents the fractions of variable AGNs as a function of their intrinsic 0.5–7 keV luminosities in different net-count bins taking into account the 12 variability-selected AGN candidates (i.e., the total number of sources is 395 + 12), where the size of each bin takes into account the need for dynamic changes in luminosity. Within the same net-count bins, the fractions of variable AGNs in bins with $L_{0.5-7\mathrm{keV,int}} > 10^{40}$ erg s^{-1} are the same within the errors. In the >500 net-count bin, the average fraction is ∼84.7%. In the 120–500 net-count bin, the average fraction is ∼38.9%. In the 30–120 net-count bin, the average fraction is ∼10.1%. These fractions are broadly consistent with the possibility that the variability of an AGN with typical variability amplitude ($\sigma \approx 30\%$–40%) can be detected given the corresponding number of net counts (see Figure 8). This result demonstrates that X-ray variability is a near-ubiquitous property of AGNs with a wide range of luminosities, confirming the previous results (e.g., Paolillo et al. 2004, 2017; Zheng et al. 2017).

One abnormally high fraction is found in the 30–120 net-count bin. The fraction of variable AGNs in the luminosity bin with $L_{0.5-7\mathrm{keV,int}} < 10^{40}$ erg s^{-1} is higher than the fractions of variable AGNs in other luminosity bins at a 95% confidence level. This significant discrepancy may be eased if we choose a different binning strategy for the luminosity bins. We also notice that there are two possible scenarios that can explain this abnormal fraction, described as follows:

[29] The sparse observing pattern of the CDF-S survey and our binning strategy may also affect our ability to detect the variability of some unidentified LLAGNs with even considerable numbers of net counts.

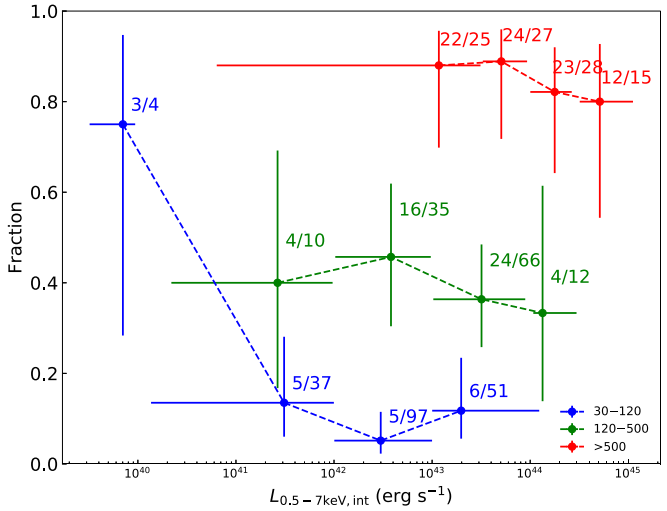

Figure 9. Fractions of variable AGNs as a function of the intrinsic 0.5–7 keV luminosities in different net-count bins for the 407 AGNs (12 variability-selected AGN candidates and 395 AGNs). The blue, green, and red points represent fractions in the net-count bins of 30–120, 120–500, and >500, respectively. The horizontal error bars indicate the width of the luminosity bin, and the vertical error bars are the binomial errors on the fractions at a 95% confidence level calculated following Cameron (2011). The labels are the ratio of the number of variable AGNs to the total number of AGNs in each bin.

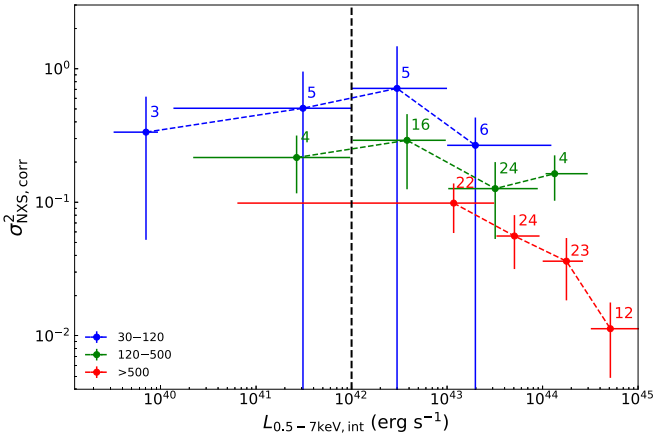

Figure 10. Medians of $\sigma^2_{\mathrm{NXS,corr}}$ vs. $L_{0.5-7\mathrm{keV,int}}$ in different net-count bins for the 148 variable AGNs (136 variable AGNs and 12 variability-selected AGN candidates). The blue, green, and red points represent the net-count bins of 30–120, 120–500, and >500, respectively. The horizontal error bars indicate the luminosity bin width, and the vertical error bars are the median of uncertainties on $\sigma^2_{\mathrm{NXS,corr}}$. The labels are the number of variable AGNs in each luminosity bin. The black dashed line is the typical LLAGN luminosity demarcation line ($L_{0.5-7\mathrm{keV,int}} \lesssim 10^{42}$ erg s^{-1} for LLAGNs).

(1) This luminosity bin includes the variable objects XID 193, XID 558, and XID 768. As discussed in Section 4.3, the possibility that XID 193 and XID 768 are ULXs cannot be ruled out. Therefore this abnormal fraction may be due to the possibility that XID 193 and XID 768 are not AGNs but ULXs, leading to an overestimation of the fraction.

(2) Within a given luminosity bin, a fraction of obscured AGNs may be missed by our sample selection because of their smaller numbers of observed net counts (after absorption) than our 30 net-count criterion. Such incompleteness is more pronounced in the low-count and low-luminosity regime. Therefore, in this low-luminosity bin, some obscured LLAGNs may be missed, leading to a significant underestimation of the denominator of the fraction of variable AGNs. In the same net-count bin (30–120 net-count bin), the fractions of variable AGNs for the other three high-luminosity bins are about the same within the errors, and the average fraction is ∼10%. Assuming that the actual fraction of variable AGNs in this low-luminosity bin equals this average value, we estimate that ∼25 obscured LLAGNs are missed in the sample selection in this low-luminosity bin.

5.3. Luminosity–Variability Relation

It has been established that X-ray variability amplitude is well anticorrelated with X-ray luminosity in high-luminosity AGNs for both short-term (less than a day, e.g., Ponti et al. 2012; Mayers et al. 2018) and long-term (month to year, e.g., Paolillo et al. 2004, 2017; Lanzuisi et al. 2014; Yang et al. 2016; Zheng et al. 2017) variability. However, the luminosity–variability relation in LLAGNs remains uncertain.

Ptak et al. (1998) studied a sample of LLAGNs observed with *ASCA* on variability timescales of less than a day, and they found that the short-term variability amplitude of LLAGNs is significantly suppressed and does not follow the luminosity–variability relation of Seyfert 1 galaxies. Subsequent studies found evidence for the short-term variability of LLAGNs being suppressed (e.g., Ptak et al. 2004; Markowitz & Uttley 2005), but some other investigations found evidence arguing against this suppression (e.g., Pian et al. 2010; Younes et al. 2011). The suppression of LLAGN short-term variability can be explained by changes in the accretion structure (e.g., Ptak et al. 1998, 2004). It is generally believed that the accretion structure in LLAGNs differs from that in high-luminosity AGNs (e.g., Lasota et al. 1996; Gu & Cao 2009; Younes et al. 2011; Hernández-García et al. 2013). In LLAGNs, accretion rates are low; the accreted material cannot be effectively cooled to collapse into a standard thin disk, and the accretion flow is advection dominated (e.g., Yuan & Narayan 2014). In this case, radiative cooling is inefficient, which causes the characteristic size of the X-ray-emitting region to be larger than that in the standard accretion structure, resulting in the suppression of LLAGN short-timescale variability (e.g., Ptak et al. 1998).

Young et al. (2012) investigated the long-term variability of LLAGN candidates found among the 4 Ms CDF-S normal galaxies. Their results indicated that the long-term variability amplitude of LLAGN candidates with $L_{0.5-8\mathrm{keV,int}} < 10^{41}$ erg s^{-1} is below the extrapolated value of the luminosity–variability relation in high-luminosity AGNs, and it is no longer inversely correlated to luminosity. However, because a few of their LLAGN candidates may be false detections, their results may be biased.

Below we investigate the luminosity–variability relation for long-term AGN variability. Figure 10 presents the medians of $\sigma^2_{\mathrm{NXS,corr}}$ versus $L_{0.5-7\mathrm{keV,int}}$ in different net-count bins for the 148 variable AGNs (136 variable AGNs and 12 variability-selected AGN candidates). In the high net-count bin (>500 counts bin), since the variability of most AGNs is detected, the medians of $\sigma^2_{\mathrm{NXS,corr}}$ unbiasedly reflect the overall variability amplitude of AGNs. In the low net-count bins (30–120 count bin and 120–150 count bin), there is a variability-detection bias (see Section 5.1) in the medians of $\sigma^2_{\mathrm{NXS,corr}}$, which leads to overestimations of the overall variability amplitude of AGNs in these bins. However, in each respective net-count bin, there is

not a significant difference in the number of observed net counts for different luminosity bins, so we do not expect that such a bias would affect the luminosity–variability trend significantly in each respective net-count bin. As shown in previous investigations of the CDF-S (e.g., Young et al. 2012; Yang et al. 2016; Paolillo et al. 2017; Zheng et al. 2017), there is an anticorrelation between the $\sigma^2_{\rm NXS,corr}$ and $L_{0.5\text{–}7{\rm keV,int}}$ in the high-luminosity regime ($L_{0.5-7{\rm keV,int}} > 10^{42}$ erg s^{-1}). However, with the decrease in luminosity, the variability amplitude of LLAGNs no longer follows the anticorrelation trend, and it appears independent of luminosity. This result is consistent with the finding of Young et al. (2012).

The observed variability amplitudes of LLAGNs may be affected by the dilution of less variable X-ray emission from XRB populations. Using the values of $L_{2-10\,{\rm keV,XRB}}$ and $L_{2-10\,{\rm keV,int}}$ obtained in Section 4.2, we calculate the $L_{2-10\,{\rm keV,XRB}}/L_{2-10\,{\rm keV,int}}$ ratios of the 12 LLAGNs in the low-luminosity bins ($L_{0.5-7{\rm keV,int}} < 10^{42}$ erg s^{-1}) in Figure 10. The lower and upper quartiles of the ratios are ≈6% and ≈49%, respectively, which suggest that the observed variability amplitudes of some LLAGNs may be underestimated to some extent. Given the limited sample size and significant uncertainties associated with $\sigma^2_{\rm NXS,corr}$ and $L_{2-10\,{\rm keV,XRB}}$, it is not feasible to quantitively constrain this effect on the luminosity–variability trend in the low-luminosity regime.

5.4. Interpreting the Luminosity–Variability Relation with an Empirical AGN Variability Model

The X-ray variability of AGNs is usually described by a PSD function that is related to the accretion rate ($\lambda_{\rm Edd}$) and black hole mass ($M_{\rm BH}$; e.g., Papadakis 2004; McHardy et al. 2006). In this scenario, the luminosity–variability relation is the consequence of the dependence of the AGN PSD on the accretion rate and black hole mass (see, e.g., Young et al. 2012; Paolillo et al. 2017; Zheng et al. 2017). Below we show that the entire observed luminosity–variability trend can be roughly reproduced by an empirical AGN variability model based on a broken power-law PSD function that is applicable universally to our sample objects. The PSD is expressed as follows (e.g., González-Martín et al. 2011):

$$\mathrm{PSD}(\nu) = \begin{cases} C(\nu/\nu_{\rm b})^{-\beta} & (\nu \leqslant \nu_{\rm b}) \\ C(\nu/\nu_{\rm b})^{-\alpha} & (\nu > \nu_{\rm b}) \end{cases}, \quad (12)$$

where $\nu_{\rm b}$ is the break frequency. McHardy et al. (2006) demonstrated that $\nu_{\rm b}$ depends on the accretion rate and black hole mass as $\nu_{\rm b} = 0.003\lambda_{\rm Edd}(M_{\rm BH}/10^6\,M_\odot)^{-1}$. Here, C is the normalization of the PSD function. Following Papadakis (2004), we assume that $C = 0.017/\nu_{\rm b}$. Also, α and β are the high-frequency and low-frequency spectral indexes, respectively. Previous studies of the X-ray variability of bright Seyfert galaxies found that $\alpha \approx 2$ and $\beta \approx 1$ (e.g., Uttley et al. 2002; Vaughan & Fabian 2003; Vaughan et al. 2003b; Breedt et al. 2009).

Given a black hole mass and accretion rate, the theoretical excess variance of an AGN can be calculated based on the above empirical AGN variability model (see, e.g., Paolillo et al. 2017; Zheng et al. 2017). Assuming that the bolometric correction factors of AGNs depend on their accretion rates and follow Equation (14) in Lusso et al. (2010), the relation between black hole mass and X-ray luminosity can be determined given an accretion rate, and then a modeled luminosity–variability relation for this given accretion rate can be derived (see, e.g., Section 5.4 of Zheng et al. 2017). Figure 11 presents the comparison of the observed data and the modeled luminosity–variability relation derived from the empirical model with $\lambda_{\rm Edd} = 0.01$–0.001. The entire observed luminosity–variability trend, including an anticorrelation in the high-luminosity regime and a plateau in the low-luminosity regime, is roughly reproduced by the empirical model. In low net-count bins (30–120 count bin and 120–150 count bin), due to the variability-detection bias, the overall variability amplitude of AGNs is overestimated, so the observed data points are higher than the modeled luminosity–variability relation. As mentioned earlier (Section 4.1), recent studies found that the low-frequency spectral index β may not be 1 and suggested $\beta = 1.2$–1.3 (e.g., Zheng et al. 2017). We note that the β value will affect the trend of the modeled luminosity–variability relation in the low-luminosity regime. However, due to the limited sample size in the low-luminosity regime and significant uncertainties associated with $\sigma^2_{\rm NXS,corr}$, it is not feasible to constrain the parameters of the PSD based on the current data.

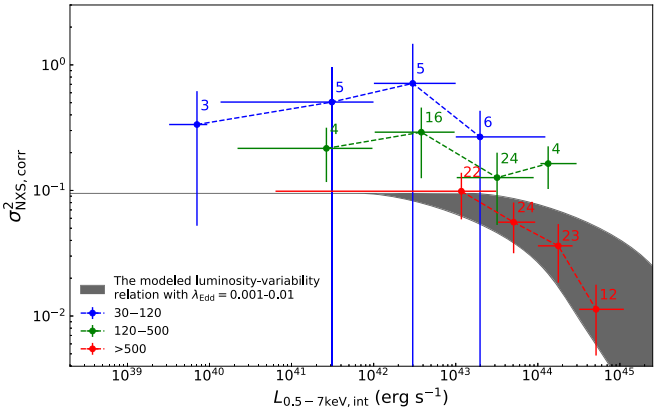

Figure 11. Comparison of the observed data and the modeled luminosity–variability relation obtained from the empirical model with $\lambda_{\rm Edd} = 0.01$–0.001. The observed data are the same as those in Figure 10. The modeled luminosity–variability relation roughly reproduces the entire observed luminosity–variability trend.

6. Summary and Future Prospects

Using the X-ray variability selection technique, we search for LLAGNs that remain unidentified among the 7 Ms CDF-S X-ray sources. The main results are summarized in the following:

1. We find 13 variable sources among 110 unclassified CDF-S X-ray sources (12^{+4}_{-2}%) using a selection criterion of $P_{X^2} < 0.015$, where P_{X^2} is the probability that the observed photon-flux fluctuation of a source is generated by Poisson noise alone. See Section 3.

2. Except for XID 869, which could be a ULX, the variability of the remaining 12 sources is most likely attributed to accreting SMBHs (i.e., AGNs). These 12 variable sources are considered as AGN candidates, of which 11 are LLAGN candidates. The redshifts of these AGN candidates range from 0.07 to 0.83. They are generally heavily obscured, with an average effective power-law photon index of about 1.8. They have low intrinsic X-ray luminosities with a median luminosity of 7×10^{40} erg s^{-1} and tend to inhabit star-forming galaxies.

Two of the 12 AGN candidates (XID 193 and XID 558) have large radio loudness and could be radio-loud AGNs. See Section 3.1.

3. Based on the simulation results of X-ray variability detection efficiency given different conditions, we find that when the total number of observed net counts is less than 100, even for an AGN with strong variability (above the average level of variability amplitude of AGNs), the probability of detecting its X-ray variability is only ∼50%. This result suggests that the 12 variability-selected AGN candidates are probably only the "tip of the iceberg" of unidentified LLAGNs in the CDF-S. See Section 5.1.

4. The fractions of variable AGNs are broadly consistent with the simulated X-ray variability detection efficiency. The fractions of variable AGNs are independent of X-ray luminosity and are only restricted by the number of observed net counts, confirming the previous findings that X-ray variability is a near-ubiquitous property of AGNs with a wide range of luminosities. See Section 5.2.

5. We confirm that there is an anticorrelation trend between X-ray luminosity and variability amplitude in high-luminosity AGNs ($L_{0.5-7\mathrm{keV,int}} > 10^{42}$ erg s^{-1}). However, with the decrease of the luminosity, the variability amplitude of LLAGNs ($L_{0.5-7\mathrm{keV,int}} < 10^{42}$ erg s^{-1}) no longer follows the anticorrelation trend, and it appears to be independent of luminosity. An empirical AGN variability model based on a broken power-law PSD function can roughly reproduce the entire observed luminosity–variability trend, including an anticorrelation in the high-luminosity regime and a plateau in the low-luminosity regime. See Sections 5.3 and 5.4.

In surveys by next-generation X-ray observatories, the X-ray variability selection technique can be used as an effective tool to select AGNs, complementing other AGN selection methods. For example, eROSITA (Merloni et al. 2012) will repeatedly survey the entire sky in the X-ray band. With the X-ray variability selection technique, eROSITA is expected to detect ∼60,000 variable AGNs in the full sky (Padovani et al. 2017). However, only a minor fraction (≪1%) of these AGNs could be LLAGNs according to the expected luminosity distribution of eROSITA-detected AGNs (Figure 5.2.3 in Merloni et al. 2012) and the reduced ability to detect the variability of low-luminosity/low-count AGNs (see Section 5.1). *Athena* (Nandra et al. 2013) has a large collecting area for detecting large numbers of X-ray photons, which makes it ideal for detecting the X-ray variability of LLAGNs. *Athena* will be able to perform X-ray surveys more than two orders of magnitude faster than *Chandra* (Nandra et al. 2013) and thus will hopefully be able to produce a sample of LLAGNs that is 100 times larger than the current CDF-S sample in an exposure time comparable to the 7 MS CDF-S. With X-ray variability measurements of large samples of LLAGNs obtained from such surveys, we will be able to better understand the properties of LLAGN X-ray variability, the luminosity–variability relation in the low-luminosity regime, and the underlying PSD form.

We sincerely thank the anonymous referee for useful suggestions. We thank Yong Shi and Dingrong Xiong for helpful discussions. We acknowledge financial support from the National Key R&D Program of China grant 2016YFA0400702 (N.D., B.L.), National Natural Science Foundation of China grant 11673010 (N.D., B.L.), NASA ADP grant 80NSSC18K0878 (W.N.B.), National Key R&D Program of China grant 2017YFA0402703 (Q.S.G.), and National Natural Science Foundation of China grant 11733002 (Q.S.G.). M.P. acknowledges support from the project "Quasars at High Redshift: Physics and Cosmology" financed by the ASI/INAF agreement 2017-14-H.0. Y.Q.X. acknowledges support from the 973 Program (2015CB857004), NSFC-11473026, NSFC-11421303, and the CAS Frontier Science Key Research Program (QYZDJ-SSW-SLH006).

ORCID iDs

N. Ding https://orcid.org/0000-0003-1028-8733
B. Luo https://orcid.org/0000-0002-9036-0063
W. N. Brandt https://orcid.org/0000-0002-0167-2453
M. Paolillo https://orcid.org/0000-0003-4210-7693
G. Yang https://orcid.org/0000-0001-8835-7722
B. D. Lehmer https://orcid.org/0000-0003-2192-3296
O. Shemmer https://orcid.org/0000-0003-4327-1460
P. Tozzi https://orcid.org/0000-0003-3096-9966
Y. Q. Xue https://orcid.org/0000-0002-1935-8104
Q. S. Gu https://orcid.org/0000-0002-3890-3729
A. M. Koekemoer https://orcid.org/0000-0002-6610-2048
C. Vignali https://orcid.org/0000-0002-8853-9611
F. Vito https://orcid.org/0000-0003-0680-9305
J. X. Wang https://orcid.org/0000-0002-4419-6434

References

Allevato, V., Paolillo, M., Papadakis, I., & Pinto, C. 2013, ApJ, 771, 9
Arnaud, K. A. 1996, in ASP Conf. Ser. 101, Astronomical Data Analysis Software and Systems V, ed. G. H. Jacoby & J. Barnes (San Francisco, CA: ASP), 17
Balestra, I., Mainieri, V., Popesso, P., et al. 2010, A&A, 512, A12
Brandt, W. N. 2005, NewAR, 49, 430
Brandt, W. N., & Alexander, D. M. 2015, A&ARv, 23, 1
Breedt, E., Arévalo, P., McHardy, I. M., et al. 2009, MNRAS, 394, 427
Broos, P. S., Townsley, L. K., Feigelson, E. D., et al. 2010, ApJ, 714, 1582
Bruzual, G., & Charlot, S. 2003, MNRAS, 344, 1000
Cameron, E. 2011, PASA, 28, 128
Cash, W. 1979, ApJ, 228, 939
Chabrier, G. 2003, ApJL, 586, L133
De Cicco, D., Falocco, S., Paolillo, M., et al. 2016, in Astrophysics and Space Science Proc. 42, The Universe of Digital Sky Surveys (Berlin: Springer), 269
Elbaz, D., Daddi, E., Le Borgne, D., et al. 2007, A&A, 468, 33
Falocco, S., Paolillo, M., Covone, G., et al. 2015, A&A, 579, A115
Feng, H., & Soria, R. 2011, NewAR, 55, 166
Garmire, G. P., Bautz, M. W., Ford, P. G., Nousek, J. A., & Ricker, G. R., Jr. 2003, Proc. SPIE, 4851, 28
Gehrels, N. 1986, ApJ, 303, 336
Giavalisco, M., Ferguson, H. C., Koekemoer, A. M., et al. 2004, ApJL, 600, L93
Gilfanov, M. 2004, MNRAS, 349, 146
Gilfanov, M. 2010, Lecture Notes in Physics, Vol. 794 (Berlin: Springer), 17
Gilfanov, M., Grimm, H.-J., & Sunyaev, R. 2004a, MNRAS, 347, L57
Gilfanov, M., Grimm, H.-J., & Sunyaev, R. 2004b, MNRAS, 351, 1365
González-Martín, O., Papadakis, I., Reig, P., & Zezas, A. 2011, A&A, 526, A132
Grogin, N. A., Kocevski, D. D., Faber, S. M., et al. 2011, ApJS, 197, 35
Gu, M., & Cao, X. 2009, MNRAS, 399, 349
Hernández-García, L., González-Martín, O., Márquez, I., & Masegosa, J. 2013, A&A, 556, A47
Ho, L. C. 2008, ARA&A, 46, 475
Hornschemeier, A. E., Alexander, D. M., Bauer, F. E., et al. 2004, ApJL, 600, L147
Kaaret, P., Feng, H., & Roberts, T. P. 2017, ARA&A, 55, 303
Kellermann, K. I., Sramek, R., Schmidt, M., Shaffer, D. B., & Green, R. 1989, AJ, 98, 1195
Koekemoer, A. M., Faber, S. M., Ferguson, H. C., et al. 2011, ApJS, 197, 36
Kroupa, P. 2001, MNRAS, 322, 231

Kurk, J., Cimatti, A., Daddi, E., et al. 2013, A&A, 549, A63
Laha, S., Ghosh, R., Guainazzi, M., & Markowitz, A. G. 2018, MNRAS, 480, 1522
Lanzuisi, G., Ponti, G., Salvato, M., et al. 2014, ApJ, 781, 105
Lasota, J.-P., Abramowicz, M. A., Chen, X., et al. 1996, ApJ, 462, 142
Lawrence, A., Watson, M. G., Pounds, K. A., & Elvis, M. 1987, Natur, 325, 694
Lehmer, B. D., Alexander, D. M., Bauer, F. E., et al. 2010, ApJ, 724, 559
Lehmer, B. D., Basu-Zych, A. R., Mineo, S., et al. 2016, ApJ, 825, 7
Lehmer, B. D., Brandt, W. N., Hornschemeier, A. E., et al. 2006, AJ, 131, 2394
Luo, B., Brandt, W. N., Xue, Y. Q., et al. 2017, ApJS, 228, 2
Lusso, E., Comastri, A., Vignali, C., et al. 2010, A&A, 512, A34
Madau, P., & Dickinson, M. 2014, ARA&A, 52, 415
Mainieri, V., Vignali, C., Merloni, A., et al. 2010, A&A, 514, A85
Markowitz, A., & Uttley, P. 2005, ApJL, 625, L39
Mayers, J. A., Romer, K., Fahari, A., et al. 2018, arXiv:1803.06891
McHardy, I. M., Koerding, E., Knigge, C., Uttley, P., & Fender, R. P. 2006, Natur, 444, 730
Merloni, A., Predehl, P., Becker, W., et al. 2012, arXiv:1209.3114
Mignoli, M., Cimatti, A., Zamorani, G., et al. 2005, A&A, 437, 883
Morokuma, T., Doi, M., Yasuda, N., et al. 2008, ApJ, 676, 121
Nandra, K., Barret, D., Barcons, X., et al. 2013, arXiv:1306.2307
Padovani, P. 2017, NatAs, 1, 0194
Padovani, P., Alexander, D. M., Assef, R. J., et al. 2017, A&ARv, 25, 2
Paolillo, M., Papadakis, I., Brandt, W. N., et al. 2017, MNRAS, 471, 4398
Paolillo, M., Schreier, E. J., Giacconi, R., Koekemoer, A. M., & Grogin, N. A. 2004, ApJ, 611, 93
Papadakis, I. E. 2004, MNRAS, 348, 207
Park, T., Kashyap, V. L., Siemiginowska, A., et al. 2006, ApJ, 652, 610
Peterson, K. C., Gallagher, S. C., Hornschemeier, A. E., Muno, M. P., & Bullard, E. C. 2006, AJ, 131, 133
Pian, E., Romano, P., Maoz, D., et al. 2010, MNRAS, 401, 677
Planck Collaboration, Ade, P. A. R., Aghanim, N., et al. 2016, A&A, 594, A13
Ponti, G., Papadakis, I., Bianchi, S., et al. 2012, A&A, 542, A83
Ptak, A., Terashima, Y., Ho, L. C., & Quataert, E. 2004, ApJ, 606, 173
Ptak, A., Yaqoob, T., Mushotzky, R., Serlemitsos, P., & Griffiths, R. 1998, ApJL, 501, L37
Richards, G. T., Lacy, M., Storrie-Lombardi, L. J., et al. 2006, ApJS, 166, 470
Santini, P., Ferguson, H. C., Fontana, A., et al. 2015, ApJ, 801, 97
Sarajedini, V. L., Koo, D. C., Klesman, A. J., et al. 2011, ApJ, 731, 97
Silverman, J. D., Mainieri, V., Salvato, M., et al. 2010, ApJS, 191, 124
Swartz, D. A., Ghosh, K. K., Tennant, A. F., & Wu, K. 2004, ApJS, 154, 519
Szokoly, G. P., Bergeron, J., Hasinger, G., et al. 2004, ApJS, 155, 271
Trevese, D., Boutsia, K., Vagnetti, F., Cappellaro, E., & Puccetti, S. 2008, A&A, 488, 73
Uttley, P., McHardy, I. M., & Papadakis, I. E. 2002, MNRAS, 332, 231
Vaughan, S., Edelson, R., Warwick, R. S., & Uttley, P. 2003a, MNRAS, 345, 1271
Vaughan, S., & Fabian, A. C. 2003, MNRAS, 341, 496
Vaughan, S., Fabian, A. C., & Nandra, K. 2003b, MNRAS, 339, 1237
Villforth, C., Koekemoer, A. M., & Grogin, N. A. 2010, ApJ, 723, 737
Vito, F., Brandt, W. N., Yang, G., et al. 2018, MNRAS, 473, 2378
Xue, Y. Q. 2017, NewAR, 79, 59
Xue, Y. Q., Luo, B., Brandt, W. N., et al. 2011, ApJS, 195, 10
Xue, Y. Q., Luo, B., Brandt, W. N., et al. 2016, ApJS, 224, 15
Yang, G., Brandt, W. N., Luo, B., et al. 2016, ApJ, 831, 145
Yang, G., Chen, C.-T. J., Vito, F., et al. 2017, ApJ, 842, 72
Younes, G., Porquet, D., Sabra, B., & Reeves, J. N. 2011, A&A, 530, A149
Young, M., Brandt, W. N., Xue, Y. Q., et al. 2012, ApJ, 748, 124
Yuan, F., & Narayan, R. 2014, ARA&A, 52, 529
Zheng, X. C., Xue, Y. Q., Brandt, W. N., et al. 2017, ApJ, 849, 127